atmosphere

MDPI

Article

The Application of an Intermediate Complexity Atmospheric Research Model in the Forecasting of the Henan 21.7 Rainstorm

Xingbao Wang [1,*], Qun Xu [1], Xiajun Deng [2], Hongjie Zhang [1], Qianhong Tang [1], Tingting Zhou [1], Fengcai Qi [1] and Wenwu Peng [1]

[1] Newsky Technology Co., Ltd., Beijing 100039, China; zhanghjcuit@163.com (H.Z.); qianhongt@aliyun.com (Q.T.)
[2] Lishui Bureau of Meteorology, Zhejiang Province, Lishui 323000, China
* Correspondence: xingbao2000@msn.com

Abstract: To improve the forecast accuracy of heavy precipitation, re-forecasts are conducted for the Henan 21.7 rainstorm. The Intermediate Complexity Atmospheric Research Model (ICAR) and the Weather Research and Forecasting Model (WRF) with a 1 km horizontal grid spacing are used for the re-forecasts. The results indicate that heavy precipitation forecasted by ICAR primarily accumulates on the windward slopes of the mountains. In contrast, some severe precipitation forecasted by WRF is beyond the mountains. The main difference between ICAR and WRF is that ICAR excludes the "impacts of physical processes on winds and the nonlinear interactions between the small resolvable-scale disturbances" (briefed as the "physical–dynamical interactions"). Thus, heavy precipitation beyond the mountains is attributed to the "physical–dynamical interactions". Furthermore, severe precipitation on the windward slopes of the mountains typically aligns with the observations, whereas heavy rainfall beyond the mountains seldom matches the observations. Therefore, severe precipitation on the windward slopes of (beyond) the mountains is more (less) predictable. Based on these findings and theoretical thinking about the predictability of severe precipitation, a scheme of using the ICAR's prediction to adjust the WRF's prediction is proposed, thereby improving the forecast accuracy of heavy rainfall.

Keywords: intermediate complexity atmospheric research model; orographic precipitation; quantitative precipitation forecasting; predictability of precipitation

check for updates

Citation: Wang, X.; Xu, Q.; Deng, X.; Zhang, H.; Tang, Q.; Zhou, T.; Qi, F.; Peng, W. The Application of an Intermediate Complexity Atmospheric Research Model in the Forecasting of the Henan 21.7 Rainstorm. *Atmosphere* **2024**, *15*, 959. https://doi.org/10.3390/atmos15080959

Academic Editor: Jordan G. Powers

Received: 27 June 2024
Revised: 6 August 2024
Accepted: 9 August 2024
Published: 12 August 2024

Copyright: © 2024 by the authors. Licensee MDPI, Basel, Switzerland. This article is an open access article distributed under the terms and conditions of the Creative Commons Attribution (CC BY) license (https://creativecommons.org/licenses/by/4.0/).

1. Introduction

From 17 to 22 July 2021, Henan Province encountered historically rare and severe heavy rain (referred to as "the Henan 21.7 Rainstorm"), resulting in severe flooding and waterlogging disasters, with especially heavy rainfall near Zhengzhou on July 20 causing significant casualties and property losses in Zhengzhou City [1]. During this extreme rain process, the daily precipitation of one-sixth of the meteorological stations in Henan Province exceeded historical extremes, among which 20 national meteorological stations, including Zhengzhou, Xinxiang, Jiaozuo, Anyang, and Hebi, exceeded the historical records since their establishment [2]. The maximum daily precipitation of 32 meteorological stations exceeded 500 mm, with 5 stations exceeding 600 mm. The maximum daily precipitation in Hebi reached 777.5 mm, and the maximum hourly rainfall at the Zhengzhou Meteorological Station reached 201.9 mm, surpassing the historical extreme value of hourly rainfall in mainland China since records began. The maximum daily precipitation was 624.1 mm, which is 3.39 times the historical maximum daily rainfall [3–5].

Precipitation is mainly associated with the vertical motion of moist air in the atmosphere. In flat areas, the necessary vertical motion for precipitation comes from the forcing of weather systems. When terrain exists, the upslope of orography against the winds can result in horizontal convergences and vertical motions of moist air and produce or enhance

precipitation. In addition to the slope of orography, the wind speed, the shear of the airflow, the slope of the orography, and the angle of intersection between the airflow and the orography also play a role. The airflow intersects with mountains more perpendicularly, and the vertical motion and its impact on precipitation become more apparent. When multi-scale weather systems interact with terrain, the vertical motion generated by the terrain becomes more complex, and the influence of terrain on precipitation becomes more intricate [6–9].

In general, precipitation generated by topographic uplift of moist air is orographic precipitation. Since the influence of terrain on precipitation is not limited to the area directly above the terrain, the distinction between orographic and non-orographic precipitation is not always clear-cut. For practical application purposes, we refer to precipitation primarily influenced by the terrain and/or occurring near the terrain as "orographic precipitation". Conversely, if precipitation is beyond orography and/or is primarily caused by the forcing of weather systems, we call it "non-orographic precipitation". Orographic precipitation accounts for a large proportion of total precipitation overland. There has been so much research on orographic precipitation, e.g., [10–21] among others. Tao [10] pointed out that extreme precipitation in China is often related to terrain. Ding et al. [11] studied heavy rainfall in Henan in August 1975 and pointed out that terrain was the key factor that caused the airflow convergence, strongly forcing lifting and storm enhancement. Chen et al. [12] analyzed the influence of terrain on heavy rain under various natural conditions, indicating that the thermal and dynamical effects of complex underlying surfaces in mountainous areas have significant impacts on the initiation, intensification, weakening, and dissipation of heavy rain. Sun [13] discussed the influence of the vertical shear of winds on precipitation on the eastern side of the Taihang Mountains in North China. They recognized that when the easterly airflow perpendicular to the mountain decreases with height, the terrain manifests the horizontal convergence and increases the cyclonic vorticity on the windward slope. Thus, the windward slope has a significant effect on the precipitation. Chen et al. [14] studied the extreme rainfall process of "7.21" in Beijing in 2012. They found that the lower-level wind field and terrain played critical roles in the triggering, intensification, and maintenance of mesoscale convective systems (MCS).

The extremely heavy rainfall of the Henan 21.7 Rainstorm was a result of the combined effects of favorable atmospheric circulation, unique geographical environment, and other factors. Western Henan is located near the Southern Taihang Mountains and Eastern Qinling Mountains, while in the western part of Zhengzhou, there are the Funiu Mountains and Songshan Mountains. The heights of these mountainous are above 500 m, and they cover a vast area. The interaction between Henan's terrain and airflows of various scales, such as low-level warm and moist easterly airflow, high-altitude westerly airflow ahead of troughs, and continuously occurring small- to medium-scale convective systems, led to this extreme heavy rainfall event. Many studies (e.g., [1–6,22,23]) have pointed out the important role of terrain in the Henan 21.7 Rainstorm.

Although many studies have been carried out on severe rainfalls, the orographic effect and its role in triggering and organizing the mesoscale convective system for the formation of severe orographic rainfall are still not fully understood. Therefore, more in-depth studies are needed to reveal the complicated mechanisms of severe orographic rainfall. In addition, to improve the accuracy of heavy rainfall forecasts, there are still many questions to be answered, for example: (1) What roles do terrain-induced lifting of airflow, physical processes, and the nonlinear interaction between resolvable-scale disturbances play in severe rainfall? (2) Does the forcing of orography impact the predictability of moist convection? (3) Are there any differences in the predictability of orographic precipitation and non-orographic precipitation? (4) Can we improve the accuracy of precipitation forecast by treating orographic and non-orographic precipitation differently according to their predictability? It is difficult to answer these kinds of questions by diagnosing the forecast using a single numerical model or by conducting sensitivity experiments (including ensemble forecasts). Instead, using atmospheric models with different dynamical complexities to simulate the same weather event can easily separate the effects of various

factors and, thus, provide answers to these types of questions. In this research, we use the intermediate complexity atmospheric research model developed by Gutmann et al. [24] (ICAR, intermediate complexity atmospheric research model) and the weather research and forecasting (WRF) model (Skamarock et al., [25]) to re-forecast the Henan 21.7 Rainstorm for a series of times. Here, the term "re-forecast" means that we use a global forecast from the NCEP Global Forecast System (GFS) like in the real forecast situation instead of using reanalysis data to generate initial values and lateral boundary conditions.

The ICAR model uses simplified dynamic methods to get the wind fields for advection. It ignores "the impact of physical-process on winds and the nonlinear interactions between the resolvable-scale disturbances" (briefly referred to as the "physical–dynamical interactions"). More discussion about ICAR can be found in Section 3.2. In the following discussion, we refer to ICAR as a "simplified dynamic atmospheric model" and correspondingly refer to the Weather Research and Forecasting (WRF) model as a "complete dynamics model" because WRF integrates the complete atmospheric dynamics equations. The complete dynamics model considers not only topographical forcing but also the impact of physical processes on the winds and the nonlinear interaction between the resolvable-scale disturbances, namely, the "physical–dynamical interactions". Therefore, the essential differences between the two models are the presence or absence of the "physical–dynamical interactions" in the model. The differences in the simulations of the complete dynamics model and the simplified dynamic model for the same weather event can help us separate the impacts of various factors, such as topography, dynamics, and physics, on precipitation. It is worth mentioning that, under the same horizontal resolution and forecast range, the computational load of the simplified dynamic model is two orders of magnitude smaller than that of the complete dynamics model.

The organization of this article is as follows: Section 2 shows the daily precipitation for a total of 6 days to illustrate the rainfall evolution before, during, and after the occurrence of the Henan 21.7 Rainstorm. The precipitation dataset for the Chinese Mainland from the Qinghai-Tibet Plateau Science Data Center (hereafter referred to as CHM_PRE; [26,27]) is used for this study. Section 3 introduces the settings of the WRF and ICAR models for our re-forecast experiments. With a 1 km grid resolution and the same finest grid, two models are used to conduct seven 72 h re-forecasts for the Henan 21.7 Rainstorm starting from 00 UTC on 17 July 2021, every 12 h. Section 4 Results: (1) presents the synoptic background that led to the Henan 21.7 Rainstorm; (2) provides visual comparisons with CHM_PRE for the precipitation forecasts of the two models; (3) explores the predictabilities of orographic and non-orographic precipitations through the potential vorticity (PV) and winds differences between WRF and ICAR; (4) discusses the predictabilities of orographic and non-orographic precipitation; (5) gives a quantitative evaluation of the precipitations from ICAR and WRF using CHM_PRE, and based on the differences in predictability between orographic and non-orographic heavy precipitation, proposes a new scheme for precipitation forecast. Section 5 presents the summary and discussion.

2. Daily Rainfall of Henan 21.7 Rainstorm

The gridded precipitation dataset CHM_PRE [26,27] is based on daily precipitation observations from a total of 2839 stations within and around China from 1961 to 2022. This dataset was obtained using the traditional precipitation ratio analysis method, combined with monthly precipitation constraints and terrain feature corrections. Here, a "precipitation ratio" refers to the ratio of daily observed precipitation at a station to the background climate field [27]. Miao et al. [26] evaluated CHM_PRE using daily precipitation data from approximately 40,000 high-density stations across China from 2015 to 2019 and found that CHM_PRE can effectively represent the spatial variations of daily precipitation. Therefore, CHM_PRE can be used for the analysis of precipitation processes and the evaluation of model precipitation.

Figure 1 shows the daily precipitation of CHM_PRE from 00 UTC on July 17 to 00 UTC on July 23. To be consistent, all times used in this research are in Coordinated Universal Time (UTC). The Digital Elevation Model (DEM) reflects the physical surface of the earth and provides the basis for the modeling and analysis of spatial-topographic information [28,29]. The DEM is essential in hydrological modeling and water cycle understanding [30]. In this study, the DEM is crucial for predicting and analyzing the impact of topography on precipitation. To indicate the relationship between the orographic height and precipitation distribution, the contours of topographic height are illustrated in Figure 1. The color shadings in Figure 1 demonstrate the main characteristics of this extreme rainfall event. On the 17th, weak rainfall centers circled with red mainly occurred near Shijiazhuang, Hebei Province, and Xinzhou, Shanxi Province, with a daily rainfall intensity of around 25 mm appearing at the junction of the Taihang Mountains in northwest Henan and the plains (Figure 1a). On the 18th (Figure 1c), the rainfall area in Hebei Province significantly expanded, with the maximum daily rainfall intensity exceeding 50 mm. Rainbands in northern Henan moved southeastward, intensifying and expanding (Figure 1b). On the 19th, precipitation intensified further, with a rainband located from the east of the Taihang Mountains in Henan to the western part of Zhengzhou where the maximum daily rainfall intensity exceeded 100 mm. A long-duration heavy rain event occurred on the 20th, with the main precipitation area in the central part of Henan and the rainfall in Zhengzhou exceeding 400 mm (Figure 1d). The extreme hourly rainfall at the Zhengzhou station reached 201.99 mm between 08 and 09 UTC on the 20th. On the 21st, the rain area moved northward to affect northern Henan and southern Hebei, with the main precipitation center exceeding 300 mm (Figure 1e). On the 22nd, the precipitation center was at the border area and the junction of Henan and Hebei, with a reduced rainfall intensity. However, the maximum intensity still exceeded 200 mm (Figure 1f). Precipitation gradually weakened after the 23rd (figure omitted). The most intense rainfall period appeared from the 20th to the 22nd. Two severe rainfall centers occurred successively in the central (Zhengzhou) and northern parts of Henan (Xinxiang, Hebi, and Anyang). Rainfall in the central part of Henan was from 00:00 on the 20th to 00:00 on the 21st, while in northern Henan, it was from 00:00 on the 21st to 00:00 on the 22nd.

Many studies ([1,2,4,22,23,31] among others) have presented the precipitation characteristics of the Henan 21.7 Rainstorm using observations from dense automatic stations. Although there are some differences between the CHM_PRE and the observations from dense automatic stations, e.g., Figure 2 in [1], the precipitation intensity and the position in CHM_PRE are consistent with their analyses.

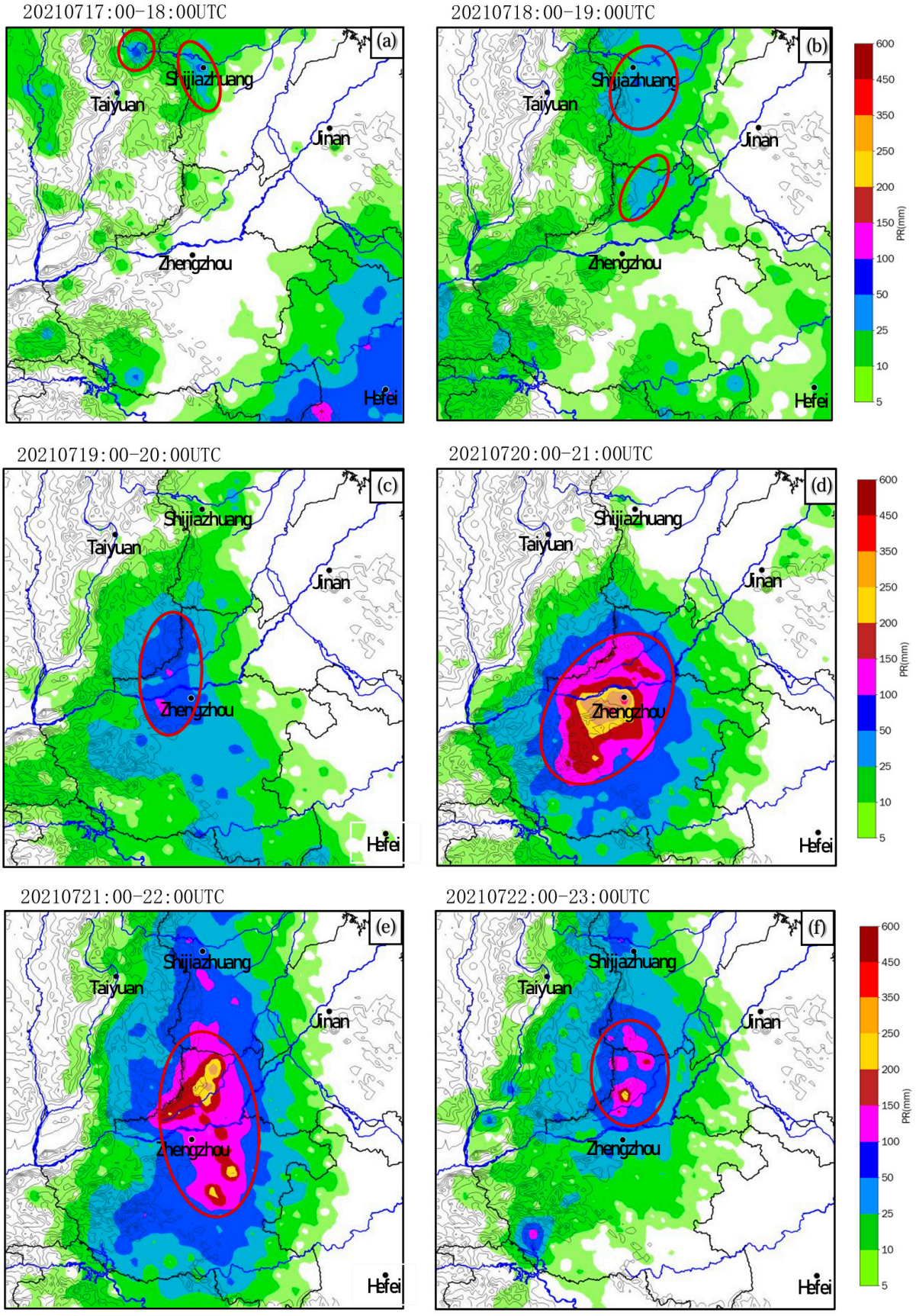


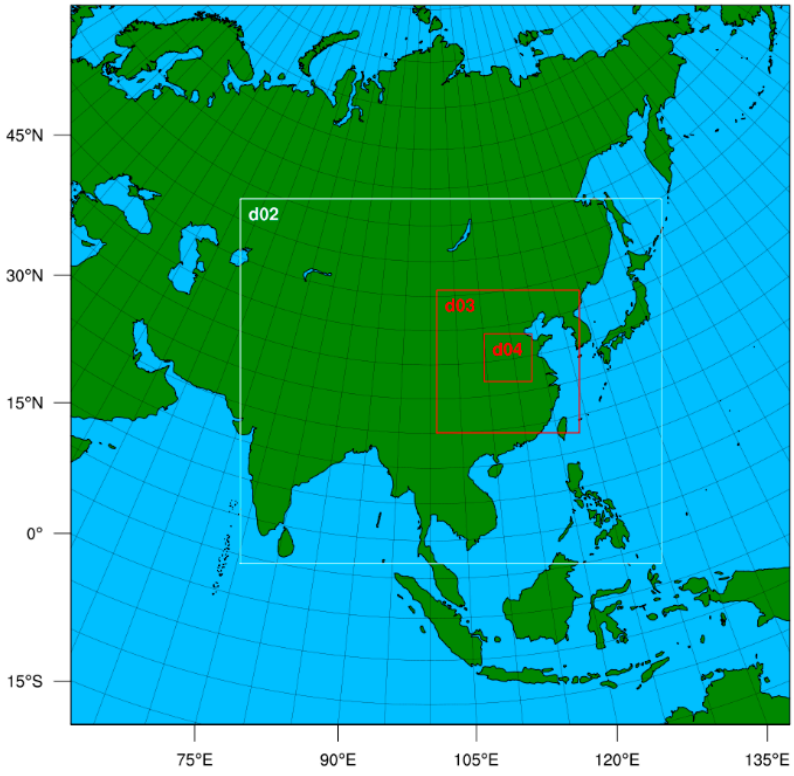
Figure 1. (**a**–**f**) The terrain height (contours, interval: 250 m) and the daily precipitation during the Henan 21.7 Rainstorm (red circles indicate the precipitation centers).

3. Model Setup

The Henan 21.7 Rainstorm was an event that occurred due to the interaction between the terrain and various weather systems of different scales. To better understand the process of how various factors like terrain forcing and dynamical and physical processes influence heavy rainfall, we conducted a series of re-forecast experiments on this extraordinary heavy rainfall event using both the mesoscale atmospheric model (WRF) and the Intermediate Complexity Atmospheric Research model (ICAR). The settings of WRF and ICAR are as follows.

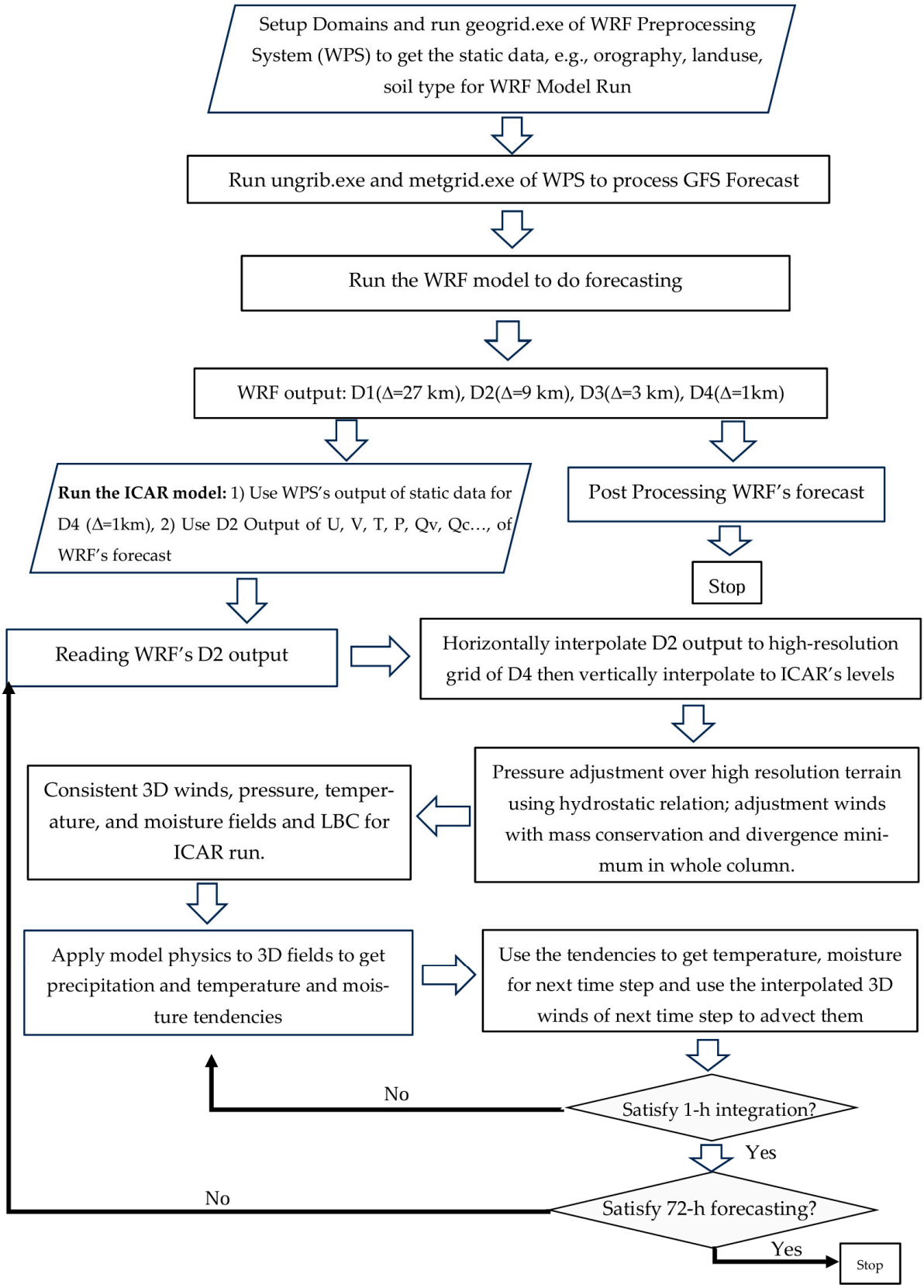
3.1. The WRF Model Setup

The WRF version 4.4.2 with the Lambert conformal conic projection (Figure 2a) and 4 domains nested is used for this study. One-way nesting is used from the coarser grid domain to the finer grid domain where the coarser grid domain provides lateral boundaries for the finer grid domain, and the results of the finer grid domain do not impact the coarser grid domain. To reduce errors introduced by the lateral boundaries, the outmost domain D01 with a horizontal grid spacing of 27 km is set to cover a large area of approximately 10,000 km east–west and 10,000 km north–south, extending from about 40° E to 160° E and from about 18° S to 81° N, with the model center at (100° E, 35° N). The second domain D02 has a horizontal grid spacing of 9 km, D03 with a horizontal grid spacing of 3 km, and D04 with a horizontal grid spacing of 1 km. Rainstorms occurred near the center of D04. The model uses 55 vertical levels with a model top at 5 hPa, approximately 30 km in height.



(**a**)

Figure 2. *Cont.*



(**b**)

Figure 2. (**a**) Four nested domains for the WRF model. (**b**) Flowchart for the WRF model and the ICAR model runs.

The integration time step for D01 is 120 s. The time step decreases in 1/3 proportion for D02, D03, and D04, becoming 40, 13.33, and 4.44 s, respectively. For D01 and D02, the Kain–Fritsch convective parameterization scheme [32] is used. Since the 3 km and 1 km grid spacing can roughly resolve convection, the convective parameterization scheme is not used for D03 and D04. The Thompson cloud physics scheme [33–35] is used for all grids. The land surface process uses the MM5 soil temperature thermal diffusion model [36–38], with a modified MM5 Monin–Obukhov scheme [39] for the near-surface layer. The YSU scheme [40] is used for the planetary boundary layer, and the RRTMG scheme [41] is used for longwave and shortwave radiation. The initial field and lateral boundary required for the model forecasts are from the NCEP GFS. The model runs in a cold start mode. The forecasts are issued at 00 and 12 UTC from 17 July 2021 to 20 July 2021, each day, with a forecast duration of 72 h.

3.2. The ICAR Model Setup

The Intermediate Complexity Atmospheric Research model (ICAR) is a simplified three-dimensional atmospheric model developed by Gutmann et al. [24]. ICAR uses a terrain-following coordinate system in the vertical direction and an Arakawa-C staggered grid in the horizontal direction. To run ICAR requires static data and forcing data. The static data refer to land use, land–sea distribution, and orographic elevation defined on latitude and longitude grids within the model's operating area. To directly compare with the high-resolution forecasts from the WRF D04, ICAR uses the static data of the WRF's fourth domain (D04) generated by the WPS (WRF, preprocessing system). ICAR uses the same physical schemes as WRF. The forcing data required by ICAR are similar to those of the Regional Climate Model (RCM), including three-dimensional temperature, pressure, humidity, and wind fields that change with time. However, unlike traditional RCMs in their use of driving data, the low-resolution forecast fields are not only used to provide lateral boundaries but also the model fields throughout the model's integration. If there are other relevant fields, such as cloud water, rainwater, ice, etc., these fields can also be input into the ICAR model through lateral boundaries. ICAR will read these data at each input time and perform linear interpolation to match the time integration within the ICAR model. ICAR can directly use atmospheric-sounding data as driving data. The flowchart of the WRF and ICAR model operation is shown in Figure 2b.

The core of the dynamic atmosphere model usually gets the wind field through the numerical solution of the Navier–Stokes equations. However, ICAR avoids directly solving the Navier–Stokes motion equations but uses simplified dynamic methods to get the wind fields above the high-resolution terrain. In this study, ICAR uses the hourly output of the WRF model at a coarse resolution (D02 at 9 km grid spacings) as the forcing data. It first interpolates the 3D temperature, pressure, humidity, and wind fields provided by the D02 grids onto a high-resolution grid (1 km grid spacing). Then, it uses the hydrostatic equation to correct the temperature and pressure fields above the high-resolution terrain and uses variational methods to adjust the wind fields under minimum whole-column mass divergence constraints with a variational method. After the adjustment of winds, ICAR can further correct the airflow above the terrain through linear mountain waves. Mountain waves are disturbances generated in stable atmospheres by terrain forcing. They are the main contribution of small-scale terrain to flow ranging from a few kilometers to tens of kilometers [18]. Mountain waves further refine the airflow forced by the terrain. The adjusted wind fields plus mountain waves are the approximate wind fields above the high-resolution terrain. To simplify the problem as much as possible, we did not use mountain wave solutions in this paper. The adjusted wind fields are interpolated linearly into 3D space at 2 min intervals. Then, the wind fields are used to transport (advect) heat, water vapor, and condensate (clouds) in the atmosphere. Thus, the precipitation and tendencies of the thermal fields are obtained through physical schemes (such as cloud physics, boundary layer, land surface, etc.) as in the complete dynamics model. ICAR is integrated in time by alternately executing calculations of physical schemes and advection. There is no difference

between ICAR and WRF except that the winds for advection calculations in ICAR come from the adjustment of the coarse resolution model's winds rather than through solving the fluid dynamics equations. In this way, ICAR ignores the impact of physical processes on the winds and the nonlinear interaction between the small resolvable-scale disturbances under high-resolution conditions. Therefore, ICAR mainly predicts precipitation due to the forcing of the high-resolution terrain on the background flow and some non-orographic precipitation due to the forcing of the coarse-resolution background flow. Due to the simplification of dynamic processes, with the same resolution as the complete dynamic atmosphere model such as WRF, ICAR's computation is 100 to 1000 times faster than that of complete dynamic atmospheric models. With our settings, the WRF model requires 120 wall-clock hours and 108 CPU cores to get a 3-day forecast, whereas the ICAR model only takes 1 wall-clock hour to finish the forecast for the same duration. Therefore, with the same computational resources, ICAR can make higher-resolution forecasts or more forecast samples, which helps better characterize the uncertainty of forecasts. In this research, we use ICAR to conduct the same forecasts as WRF, from 17 July 2021 to 20 July 2021, with a 72 h forecast made daily at 00 and 12 UTC.

The simplified dynamics of ICAR essentially turn it into a linear model. One of the key characteristics of a linear model is that various components satisfy the superposition principle. It is easy to separate orographic precipitation from the non-orographic precipitation in the ICAR model. In contrast, there may be an interaction between orographic precipitation and non-orographic precipitation due to the "physical–dynamical interactions" in the WRF model. If the orographic precipitation predicted by ICAR is similar to the orographic precipitation predicted by WRF, we can conclude that the action of the "physical–dynamical interactions" in the WRF model is not significant in the process of orographic precipitation. Thus, we can approximately separate the orographic precipitation from the non-orographic precipitation in the WRF model through ICAR's precipitation.

4. Results

4.1. The Synoptic Background That Caused the Henan 21.7 Rainstorm

Ding [42] listed the conditions for sustained severe MCS: (1) strong water vapor convergence in the lower atmosphere; (2) strong upward motion in the mid-troposphere; (3) constant rebuilding of potential instability; and (4) favorable terrain forcings. To check whether these conditions are met in the Henan 21.7 Rainstorm, first, we analyze the large-scale weather situation.

4.1.1. Sea-Level Pressure and Orographic Height

Figure 3a–d shows the forecasts at 0, 1, 2, and 3 days from D02 of the WRF model initialized on 00 UTC, July 19, 2021. The figure depicts sea-level pressure (contours), 10 m winds (barbs), and the terrain height (shaded). At the starting time, Typhoon Cempaka was in the South China Sea, then it moved toward the Guangdong coast and gradually intensified. After 21 July, it made landfall and weakened gradually, appearing as a weak low-pressure system on July 22. Typhoon In-Fa was significantly stronger than Typhoon Cempaka over the eastern ocean of Taiwan on 00 UTC, 19 July 2021. There existed a strong pressure gradient and westward airflow between In-Fa and the subtropical high-pressure system, which was near the Sea of Japan. Over time, Typhoon In-Fa intensified and moved westward. The westward airflow in between subtropical high and Typhoon In-Fa was strengthening and extending westward. The shadings in Figure 3 show the terrain characteristics surrounding Henan: the eastern part is the alluvial plain between the Huaihe River and the Yellow River, while the southwest of Zhengzhou has the Songshan, Funiu, and Qinling Mountains and the northwest has the Taihang Mountains. When the warm and moist westward airflow carrying a large amount of water vapor encountered the terrain of western Henan, the terrain uplifted the westward airflow, which led to upward motion and severe orographic precipitation.

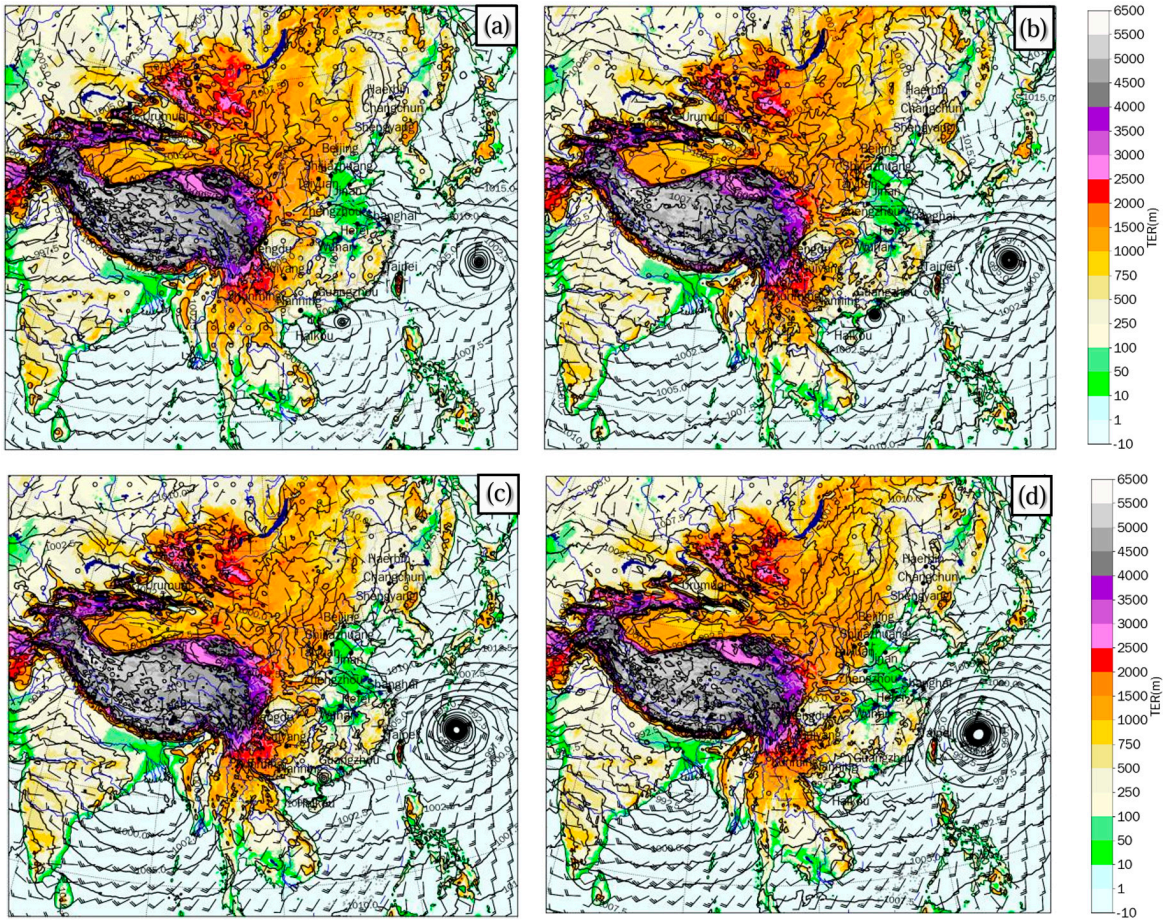


Figure 3. (**a**–**d**) represents the surface pressure and wind field obtained for the forecast at 0, 1, 2, and 3 days, respectively, starting from 00 UTC, 19 July 2021. The color shadings show the terrain height.

4.1.2. The 850 hPa Height and Precipitable Water

Figure 4 shows the evolution of geopotential height (contours, units in 10 gpm), winds (barbs), and atmospheric precipitable water (shading, in units of kg m^{-2}) on the 850 hPa pressure surface. The atmospheric precipitable water indicates a high humidity zone from Wuhan to Zhengzhou and Shijiazhuang, with maximum values exceeding 65 kg m-2 near Zhengzhou. Sun et al. [43] analyzed the causes of extreme precipitation in Beijing on 21 July 2012. They found that abnormally high water vapor content (with precipitable water reaching 60–80 mm) is a crucial condition for extreme precipitation. Xu et al. [44] analyzed a typical heavy rain event in the warm sector of a midlatitude cyclone between the Huang River and the Huai River on 17 July 2012. They found that a high-humidity environment throughout the troposphere increases precipitation efficiency, reduces lifting condensation levels, and favors the repetitive generation of MCS. Typhoon Cempaka, located on Guangdong's coast, transported water vapor inland with a southerly airflow on its eastern side. The easterly airflow associated with the strong pressure gradient between Typhoon In-Fa and the subtropical high pressure system near the Japan Sea also transported water vapor from the ocean toward Henan Province. The synoptic background provided abundant moisture for the Henan 21.7 Rainstorm [31,45]. The two moisture conveyor belts converged in central-western Henan where the obstruction of the Taihang Mountains and Song Mountains exists. Buhe et al. [46] found that during the extreme precipitation on 20 July, the meridional moisture flux in southern Henan enhanced significantly. The enhanced flux provided more moisture for the extreme rainstorm.

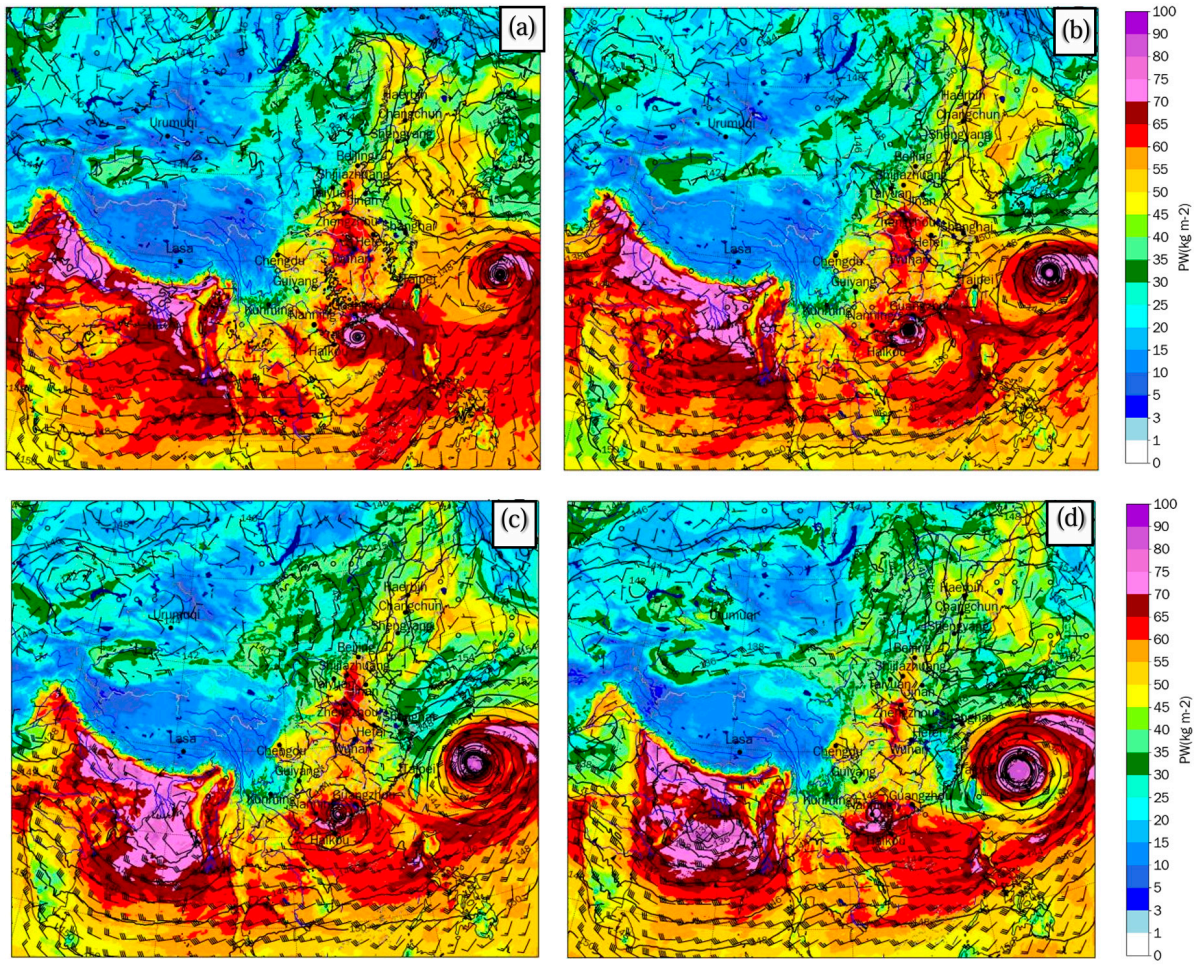


Figure 4. (**a**–**d**) represents the surface pressure and wind field obtained for the forecast at 0, 1, 2, and 3 days, respectively, starting from 00 UTC, 19 July 2021. Same as Figure 3 but shows the geopotential height (contours), winds (barbs), and atmospheric precipitable water (shadings) on the 850 hPa pressure surface.

4.1.3. The 500 hPa Height and Temperature

Figure 5 shows the evolution of the geopotential height, winds, and temperature in the middle troposphere. There was a quasi-steady cold trough over the north Lake Balkhash and the west of Lake Baikal. The pressure ridge from the Qinghai-Tibet Plateau to Ningxia and Inner Mongolia was reinforced gradually and extended eastward. The North Pacific subtropical high extended westward from the Sea of Japan to the east-central region of China. A shortwave trough splitting off the quasi-steady cold trough was moving southeastward from the southwest of Lake Baikal, which indicated a small burst of cold air moving south that might uplift moist warm air to produce precipitation. There was a wide low-pressure zone between the Yellow River and the Huai River. Meanwhile, Typhoon Cempaka was in the South China Sea and Typhoon In-Fa was in the Eastern Ocean. From a macro perspective, the east-central region of the mainland was within a wide and broad saddle region. This synoptic background led to the precipitation systems occurring in Henan within a relatively less-moving atmospheric environment.

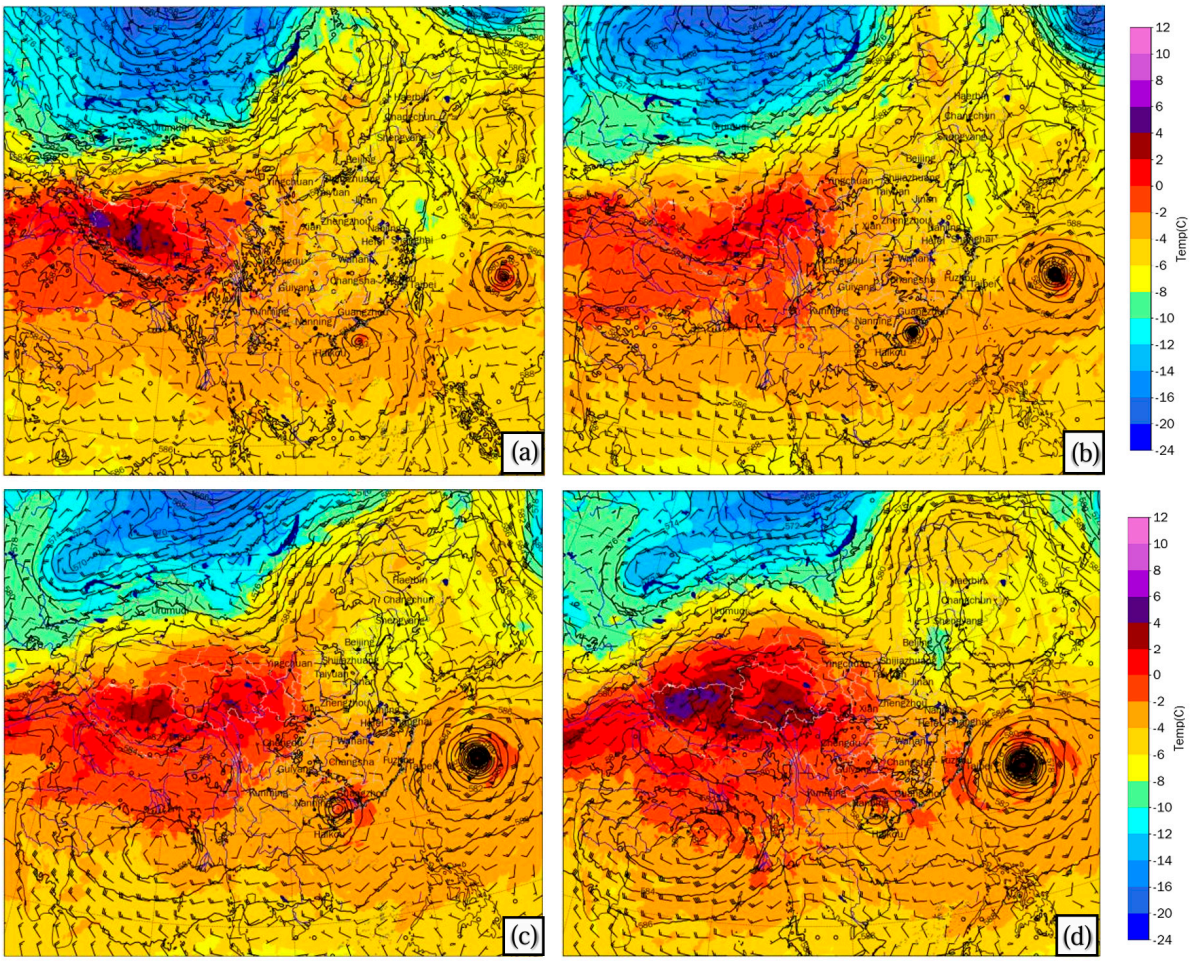


Figure 5. (**a**–**d**) represents the surface pressure and wind field obtained for the forecast at 0, 1, 2, and 3 days, respectively, starting from 00 UTC, 19 July 2021. Same as Figure 3 but shows the geopotential height (contours), winds (barbs), and temperature (shadings) on the 500 hPa pressure surface.

4.1.4. The 200 hPa Height and Potential Vorticity

Figure 6 shows the evolution of geopotential height, winds, and potential vorticity (PV, shading) on the 200 hPa pressure surface. A wide positive PV area (corresponding to a cold trough) extended from northern Xinjiang to the west of Lake Baikal. There was a negative PV zone from Lake Baikal to Inner Mongolia, which corresponded to the strong shear on the left side of the jet stream in front of the 200 hPa trough. The negative PV over the Qinghai-Tibet Plateau corresponded to the Qinghai-Tibet High, which gradually strengthened and extended northeastward from the 19th to the 22nd. Furthermore, there was a positive PV zone (corresponding to the weak trough) in the east of the Qinghai-Tibet high, extending across Yunnan, Sichuan, Ningxia, and Inner Mongolia. Under the influence of the northeastward flow in the southeast of Qinghai-Tibet high and the southwest flow ahead of the weak trough in eastern Inner Mongolia, the PV zone was gradually stretched into a narrower PV band from the northeast to the southwest. The PV value above Zhengzhou changed gradually from positive to negative from the 19th to the 21st. Meanwhile, the positive PV on the 850 hPa near Zhengzhou gradually strengthened. From the 19th to the 20th, the water vapor was transported continuously by the low-level jet stream to central and western Henan [31]. The heavy rainfall occurred in west and central Henan under the condition of uplifting the easterly airflow by the terrain along with the latent heat releasing in the middle and lower troposphere. According to the principle of PV conservation [47–49], the PV increased below (decreased above) the maximum heating layer in the troposphere. The PV redistribution resulted in anticyclonic vorticity in the

upper troposphere and cyclonic vorticity in the lower troposphere. The redistribution of PV strengthened the MCS in central and western Henan.

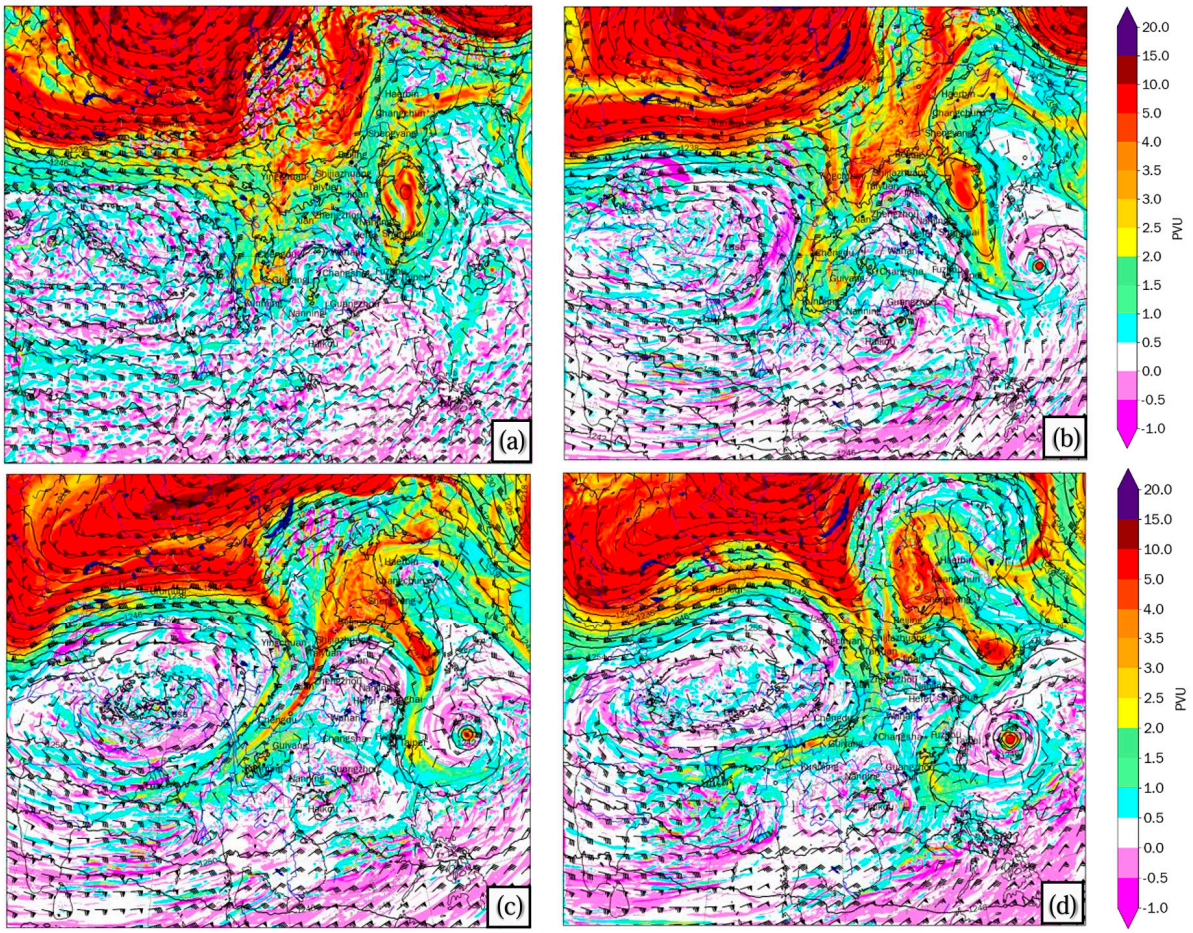


Figure 6. (**a**–**d**) represents the surface pressure and wind field obtained for the forecast at 0, 1, 2, and 3 days, respectively, starting from 00 UTC, 19 July 2021. Same as Figure 3 but shows the geopotential height (contours), winds (barbs), and potential vorticity (shading) on the 200 hPa pressure surface.

4.2. Reliability of Forecasting and Predicatability

4.2.1. The 3-Day Accumulative Precipitation

We have discussed the synoptic backgrounds that led to the Henan 21.7 Rainstorm. Now we pay attention to precipitation forecasts and their reliability. At first, we evaluate the 3-day total precipitation predicted by the WRF and the ICAR models with CHM_PRE as an observation. In this subsection, we assess the precipitation through visual comparison with the observation. Figure 7a–c shows the 3-day total precipitation in CHM_PRE and the forecasts of WRF and ICAR from 00 UTC on July 19 to 00 UTC on July 22. Figure 7d shows the terrain height in D04. The extreme rainfall of the Henan 21.7 Rainstorm occurred during this period. The precipitation forecasts for other times can be seen in the supplementary materials.

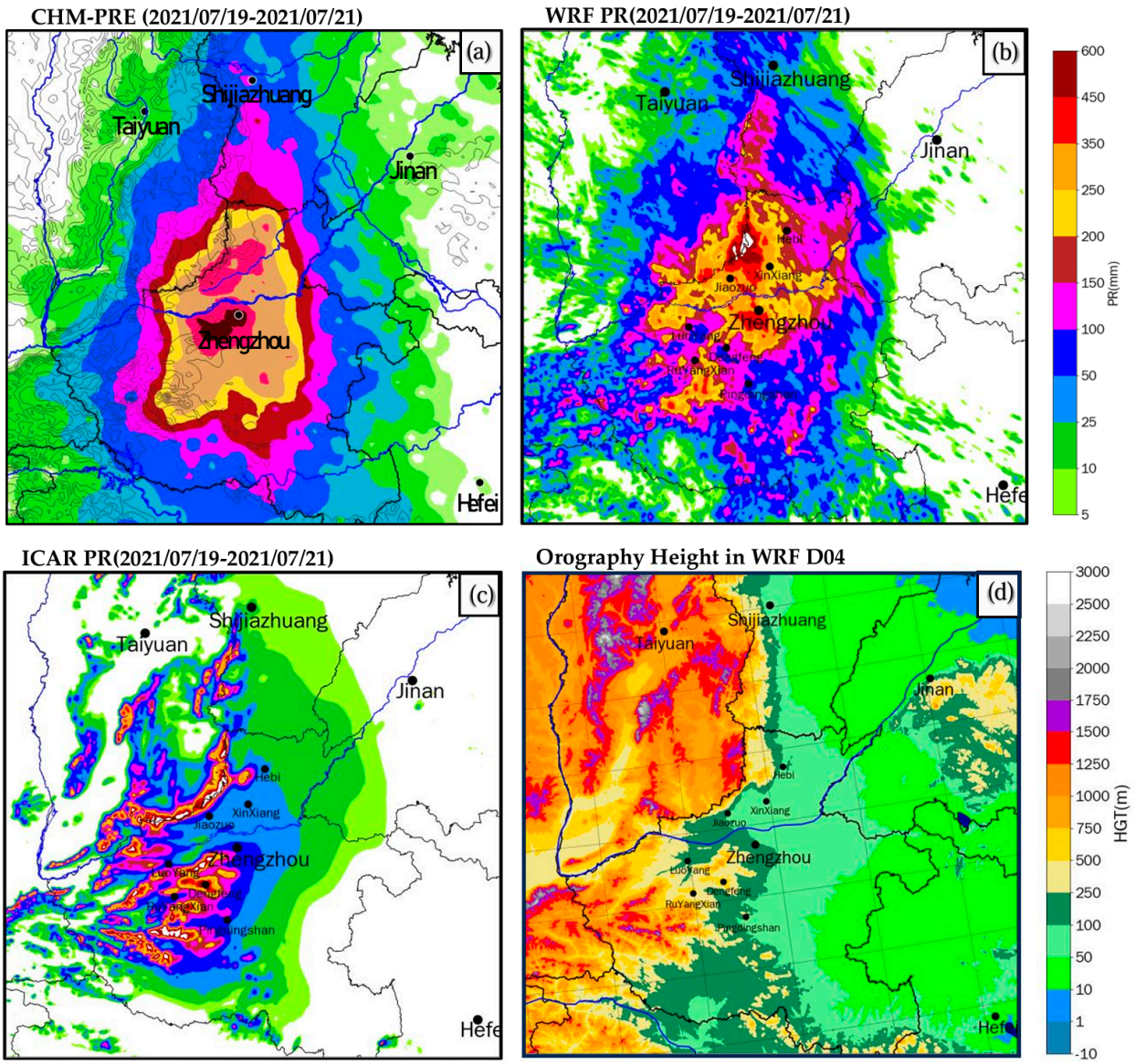


Figure 7. The 3-day accumulative precipitation of (**a**) CHM_PRE, (**b**), and (**c**) are precipitation forecasts from WRF and ICAR; (**d**) displays the terrain height.

There are two heavy precipitation regions in Figure 7a. One is a wide precipitation band with 450–600 mm rainfall between Zhengzhou and Luoyang. The other is a precipitation band stretching from Hebi to Xinxiang and Jiaozuo north of the Yellow River, with rainfall of 350–450 mm. Both severe precipitation bands are situated on the windward slopes of mountains or in the transition zones between mountains and plains. The precipitation distribution strongly suggests the impacts of the terrain. Figure 7b shows the 72 h precipitation forecast from the WRF model. There are two precipitation bands also. One is situated near Zhengzhou, with precipitation of 350–450 mm. The area with rainfall exceeding 350 mm is significantly smaller than CHM_PRE in Figure 7a. Another precipitation band is situated on the east slope of the Taihang Mountains at the border of Henan and Shanxi, with a maximum rainfall exceeding 600 mm, which is heavier than CHM_PRE. Correspondingly, the distribution of heavy precipitation in Figure 7c (from ICAR) is in a narrow band, which inclines toward the windward slopes of the terrain or flared valleys. The area with precipitation exceeding 350 mm in Figure 7c is much smaller than CHM_PRE and WRF. However, the severe precipitation of ICAR indicates that the southwest of Zhengzhou experienced greater precipitation. It is very much in line

with observations. In addition, the severe precipitation on the east slope of the Taihang Mountains coincides with the region of large gradient of terrain height (cf. Figure 7d). In the area beyond the terrain, ICAR's precipitation is only 5–25 mm and in a wider range. It is noticeably weaker than WRF's precipitation.

The difference between Figure 7b,c can be attributed to the presence or absence of the "physical–dynamical interactions." The key point is that the ICAR model neglects the actions of physical processes on the winds, e.g., the latent heat released by condensation increases mid-level vertical motion, and the vertical motion enhances the low-level convergence. If the location and intensity are correct, the "physical–dynamical interactions" do make the precipitation distribution appear more similar to the observed precipitation (Figure 7a vs. Figure 7b). However, the heavy rainfall beyond the terrain in the WRF model has no clear correspondence with the observations in location and intensity. On the other hand, the ICAR's heavy rainfall in the west of Zhengzhou and along the Taihang Mountains is quite consistent with the observation in Figure 7a. This fact indicates the simple dynamical model captures the features of the orographic precipitation. Moreover, the differences between the complete dynamical model and the simplified dynamical model can help us understand the impacts of complex terrain and the "physical–dynamical interactions" on precipitation. ICAR's precipitation provides us with an important reference to distinguish the orographic and non-orographic precipitation.

Many studies [1–6,16,18,23] have analyzed the Henan 21.7 Rainstorm and its relationship with the terrain. Among them, Zhang et al. [4] found that during the Henan 21.7 Rainstorm, 400–800 mm precipitation accumulated from 00 UTC on 16 July to 00 UTC on 23 July concentrated near the eastern foot of the Taihang Mountains, the windward slopes of the Funiu Mountains, or flared valleys. Only a few stations in the plains had heavy precipitation. Two heavy rainfall centers exceeding 800 mm are adjacent to the Taihang Mountains in northern Henan and along the eastern side of the Funiu Mountains in the west of Zhengzhou. Wang et al. [31] found that under the combined effect of large-scale thermal and dynamic blocking, the heavy rainfall ultimately presented a distribution pattern on the windward slopes of the terrain. Zhang et al. [22] pointed out that the low-level airflow blocked by the Taihang Mountains and the strong convergence of water vapor flux on the eastern side of the terrains was conducive to the continuous merging and development of newly formed convective cells. As a matter of fact, this kind of rainfall distribution is not rare. Many studies have demonstrated the importance of terrain in the formation of severe rainstorms. For example, Li et al. [50] analyzed the "7.19" extreme rainstorm in 2016 with accumulative rainfall exceeding 250 mm near the eastern foot of the Taihang Mountains. They found that rainfalls exceeding 500 mm were all located at elevations above 300 m. Our results are consistent with their findings.

4.2.2. The Daily Cumulative Precipitation

In this subsection, we evaluate the daily precipitation forecasts by WRF and ICAR with CHM_PRE's. Figure 8 presents the accumulative precipitation from WRF and ICAR for 0–24 h, 24–48 h, and 48–72 h from 19 July 2021, 00 UTC. The plots of accumulative precipitation forecasts from 17 July 2021 to 20 July 2021 can be found in the Supplemental file. For the convenience of direct visual comparison, we place CHM_PRE's precipitation analysis on the left side. Figure 8a–c shows that on the 19th (from 00 UTC on the 19th to 00 UTC on the 20th, and so forth), areas with precipitation intensity exceeding 50 mm are mainly situated to the west of Zhengzhou and to the east of the southern Taihang Mountains. Additionally, there are localized heavy rainfalls (daily precipitation of 100–150 mm) near Luoyang. The precipitation center on the 20th is located in Zhengzhou and nearby areas, with the maximum daily precipitation ranging from 350 mm to 450 mm. By the 21st, the precipitation center moves northward, with severe rain distributed in northern Henan and along the east slope of the Taihang Mountains. The severe precipitation band is along the line from Hebi to Xinxiang and Jiaozuo, in which the daily precipitation values range from 250 mm to 350 mm. The most intense precipitation of this rainstorm occurred

on the 20th, with the precipitation center near Zhengzhou. The maximum hourly precipitation at the Zhengzhou meteorological station occurred on the 20th [2,4,31]. Figure 8 illustrates that the daily precipitation forecasts from WRF and ICAR generally replicate the intense precipitation processes near Zhengzhou and the Taihang Mountains. However, for the extreme precipitation events near Zhengzhou and the Taihang Mountains, there are deviations between the forecasts and actual observations. Additionally, the precipitation intensity and range forecasted by the two models are also different.

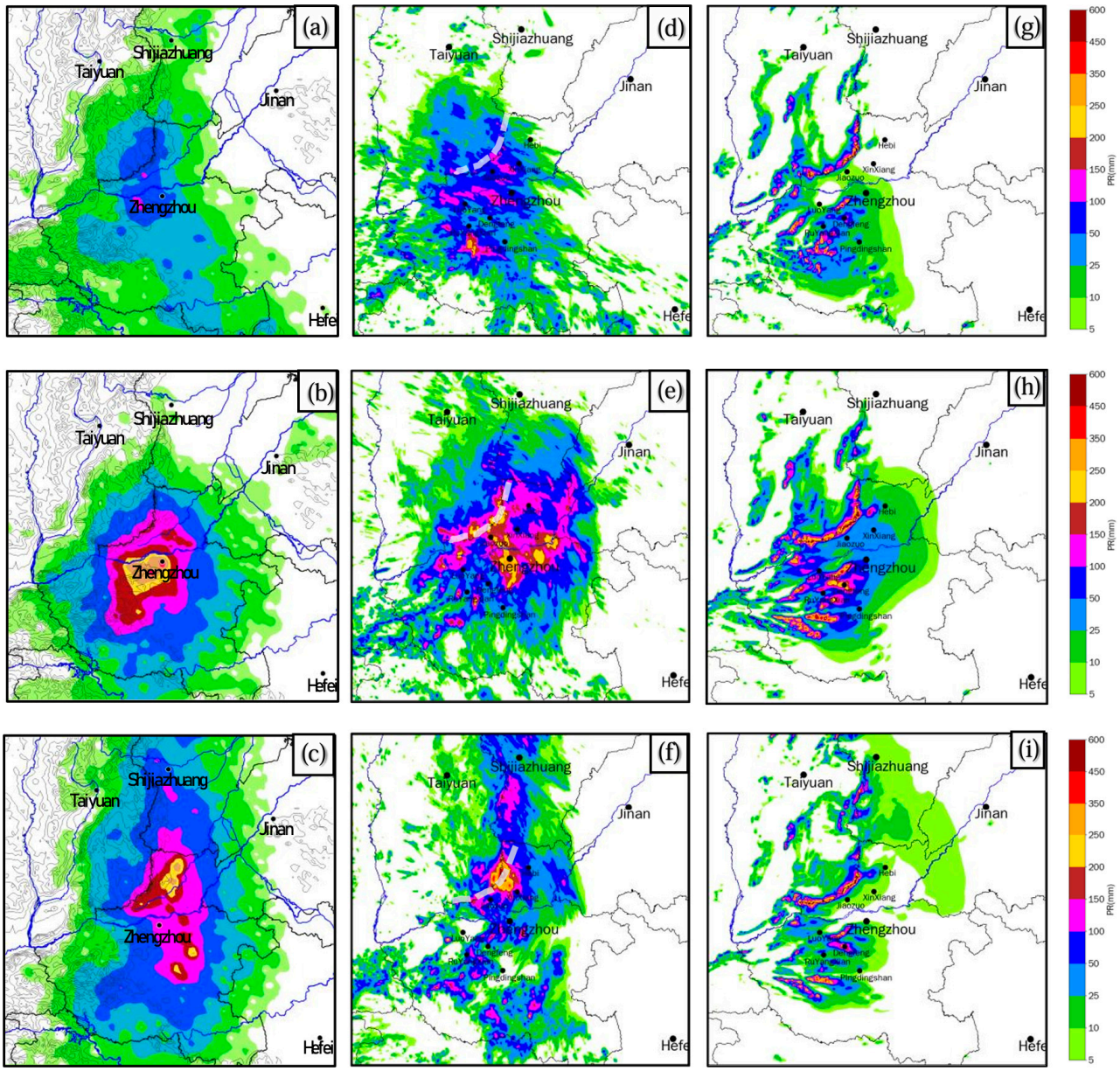


Figure 8. (**a**–**c**) shows the 24 h accumulative precipitation of CHM_PRE, while (**d**–**f**) depicts the first, second, and third day accumulative precipitation forecasted by WRF, and (**g**–**i**) represent the first, second, and third day accumulative precipitation forecasted by ICAR. Both models are initialized at 00 UTC on 19 July 2021. The gray dashed lines in (**d**–**f**) correspond to the precipitation bands on the slope of the Taihang Mountains in (**g**–**i**).

Figure 8d shows the 0–24 h precipitation forecast from the WRF model. Compared with the observations (Figure 8a), the area of precipitation exceeding 5 mm in the WRF forecast is smaller than CHM_PRE. However, the area of precipitation exceeding 25 mm

in Figure 8d is significantly larger than CHM_PRE. Additionally, several scattered heavy precipitation centers are deviating far from the terrain. The maximum daily precipitation in the WRF forecast exceeding 200 mm is in the south of Ruyang County, but there is only 10–20 mm precipitation in CHM_PRE (Figure 8a) at the same place. Furthermore, the precipitation center in Figure 8a is near Luoyang with a maximum of 150 mm only. The total area of precipitation exceeding 5 mm in the ICAR forecast (Figure 8g) is smaller than WRF, and the area of precipitation above 50 mm is similar to that of CHM_PRE. The region with precipitation above 100 mm tends to be on the windward slope of the terrain. Outside the intense precipitation, there is a wide range of 5–25 mm precipitation area in Figure 8g, which is related to the background forcing. Compared with WRF, the precipitation due to background forcing is much weaker. As we have mentioned earlier, this is mostly due to the neglect of the action of physical processes on wind in ICAR. Compared with the terrain height in Figure 7d, it is easy to find that the intense precipitation in Figure 8g coincides with the height gradient on the windward slope of the terrain. Therefore, the intense precipitation in the ICAR model is mainly due to terrain forcing. Comparing Figure 8d with Figure 8g, we can find that the precipitation in WRF is slightly toward the mountain front rather than the mountainside as in ICAR. The hourly precipitation (figure omitted) from the WRF model shows the continuous emergence of small and medium-sized rain clusters from southeast to northwest or from south to north. However, the hourly precipitation in the ICAR model mainly congregates along the windward slope of the terrain. The hourly precipitations in the WRF prediction are quite similar to the analysis in [1–6]: The rainfall during the Henan 21.7 Rainstorm was primarily caused by a meso-α (horizontal scales L~200–2000 km) scale convective system characterized by a nearly circular structure spanning about 300 km horizontally. The longtime presence of this meso-α system was linked to the merging of several meso-β (L~20–200 km) scale convective systems within it and the train-like continuous coming up of single-cell systems from the warm and moist areas on its southeastern periphery. They also highlighted that the extreme hourly precipitation (201.9 mm h^{-1}) in Zhengzhou was mainly due to the development of a very strong meso-γ (L~2–20 km) scale convective system located on its southwest side. Wang et al. [15] studied extreme heavy precipitation weather with hourly rainfall exceeding 50 mm on the eastern foot of the Taihang Mountains under two different weather backgrounds. They pointed out that the easterly flow and downslope thunderstorm outflow can form a mesoscale convergence line that triggers new thunderstorms. Radar echoes showing backward propagation characteristics and the effect of deep convection sequences that pass one after another like trains cause local extreme short-duration heavy precipitation.

Figure 8e,h shows the 24–48 h cumulative precipitation forecasts from WRF and ICAR. The total areas of precipitation exceeding 5 mm in both forecasts are smaller than that in CHM_PRE. The heavy precipitation forecast from the ICAR remains in bands, mainly distributed on the windward slopes of the terrains. The area of precipitation exceeding 50 mm in the ICAR model is comparable to CHM_PRE. The area of precipitation exceeding 50 mm in the WRF is larger than CHM_PRE. In Figure 8e, multiple daily precipitation centers exceeding 200 mm are distributed along the eastern foothills of the Taihang Mountains and near Zhengzhou. However, the precipitation in the west of Zhengzhou is heavier than in the east of Zhengzhou. In addition, Figure 8e shows that two precipitation centers exceeding 200 mm in northeast Zhengzhou along the Yellow River are absent in the 24–48 h precipitation of ICAR (Figure 8h). Therefore, the two severe precipitation centers in Figure 8e are due to the "physical–dynamical interactions". Such severe precipitation centers do not appear in CHM_PRE (Figure 8b); therefore, the severe non-orographic precipitation due to the "physical–dynamical interactions" does not align with the observation.

Figure 8f,i shows the 48–72 h precipitation forecasts from WRF and ICAR. Still, the area with precipitation exceeding 5 mm in the WRF model is smaller than in CHM_PRE. Figure 8i indicates that precipitation forecasted by the ICAR model remains in the band structure, with a smaller area of heavy precipitation than in the WRF model. The precipitation center is also concentrated on the windward slope of the terrain. The thick gray dashed lines in Figure 8d–f respectively correspond to the severe precipitation band along the eastern side of the Taihang Mountains in Figure 8g–i. Comparing Figure 8d–f with Figure 8g–i, we can find that the precipitation over the east of the Taihang Mountains in the WRF model corresponds well with the precipitation band in the ICAR model and CHM_PRE. In other words, the terrain-induced precipitations in the complete dynamic model and the simplified dynamic model have a good correlation with the observation. Furthermore, from Figure 8g–i, we can see that the terrain-induced precipitation in the ICAR model does not change much over time, indicating that terrain-forced precipitation is relatively insensitive to changes in the background airflow. This, on the other side, demonstrates that terrain-induced precipitation has better predictability.

Based on the above analyses, we can conclude that the predictability of severe precipitation induced by terrain is higher than that of severe precipitation produced by the "physical–dynamical interactions". The main differences in precipitation between WRF and ICAR are due to the "physical–dynamical interactions". Without considering errors such as precipitation phase and intensity, the "physical–dynamical interactions" make the precipitation forecast in WRF look more like observations, but unfortunately, that does not guarantee it is consistent with actual precipitation.

4.2.3. The Reliability of Severe Precipitation Prediction

To understand the impacts of topography and the "physical–dynamical interactions" on the severe precipitation and the reliability/predictability of the Henan 21.7 Rainstorm, we conduct further analyses of the MCS associated with precipitation. Figure 9a–f displays wind fields at 2 km, 5.5 km, and 8.5 km heights for the 36 h lead time (at 12 UTC on 20 July 2021) of WRF and ICAR. The shading illustrates the accumulative precipitation from 24 h to 36 h. Figure 9a–c is from the ICAR model, while Figure 9d–f represents the WRF model. Figure 9 reveals that the winds over Henan flow predominantly southeast at 2 km height, transitioning to southerly flow at the middle level (5.5 km) and westerly flow at the upper level (8.5 km). A cyclonic vortex is observed in the mid-level troposphere (5.5 km) over Shanxi Province. Figure 9a–c suggests that the spatial variation of the winds predicted by the ICAR model is relatively smooth, whereas Figure 9d–f exhibits more fluctuations. The white contour lines in Figure 9 representing the vertical velocity of 1, 2, and 3 ms^{-1} illustrate the distribution of strong vertical motions. In the ICAR model (Figure 9a–c), the strong vertical motions are primarily on the windward slopes of the terrain, and vertical velocity diminishes relatively slowly with the height. In contrast, the strong vertical motions near the terrain in the WRF model (Figure 9d–f) are more on the lower and middle levels of the troposphere. Additionally, beyond the terrain, there are strong vertical motions that are associated with freely developing mesoscale convective systems. The white contour lines reflect the relationship between precipitation and vertical velocity approximately. With shorter time intervals, heavy precipitation and vertical velocity align more closely, indicating that areas of heavy precipitation generally coincide with a strong upward motion (figure omitted). Therefore, the heavy precipitations beyond the mountains in Figure 9d–f are associated with severe moist convection.

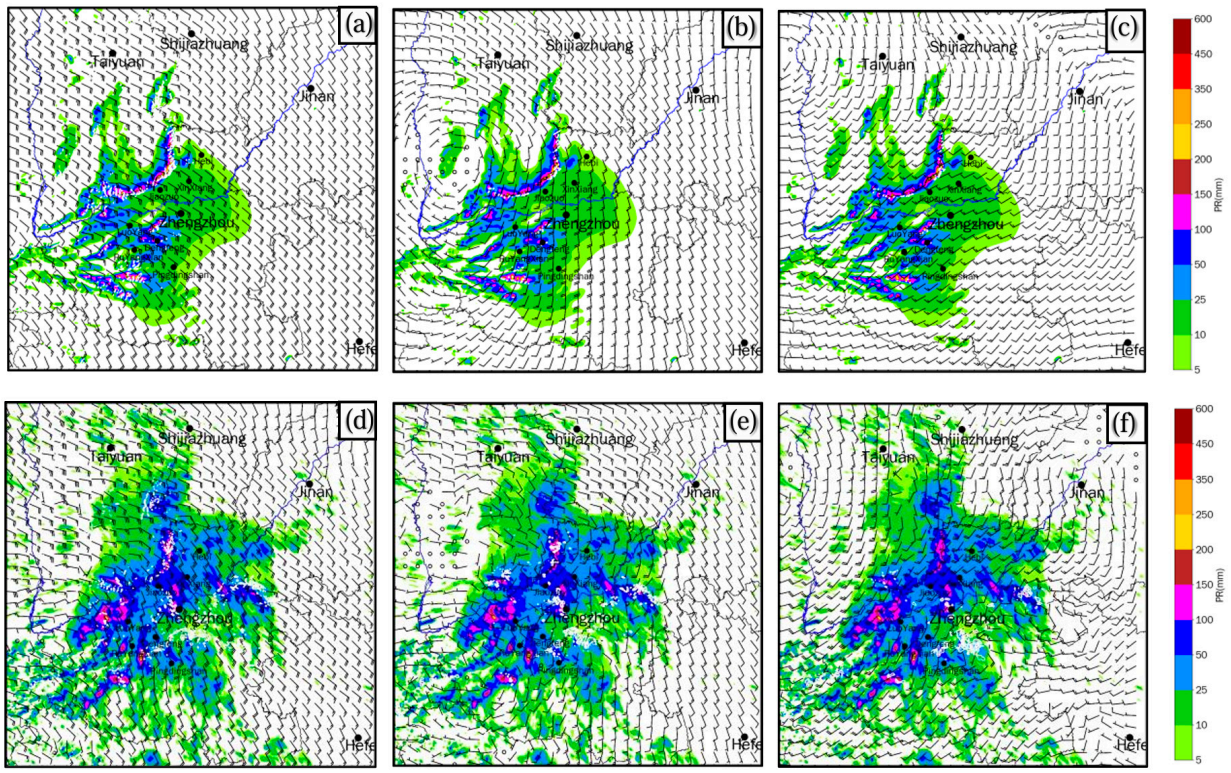


Figure 9. The 36 h wind field (barbs) at 2 km, 5.5 km, and 8.5 km heights and the 12 h accumulative precipitation (color-filled) from 00 to 12 UTC on 20 July 2021, with models starting from 00 UTC on 19 July: (**a**–**c**) ICAR; (**d**–**f**) WRF. Additionally, the white contour lines represent instantaneous vertical velocities of 1, 2, and 3 m s^{-1} at the 36 h lead time.

According to the principle of PV conservation [47–49]:

$$\frac{dPV}{dt} = \frac{\partial PV}{\partial t} + \vec{V}\cdot\nabla PV = \frac{1}{\rho}\vec{\xi_a}\cdot\nabla\dot{\theta} + \frac{1}{\rho}\bigtriangledown\times\vec{F}\cdot\nabla\boldsymbol{\theta}, \quad (1)$$

where $PV = \rho^{-1}\vec{\xi_a}\cdot\nabla\theta$, ρ, air density, $\vec{\xi_a}$, the absolute vorticity, θ, potential temperature, $\vec{V}$, the winds, $\vec{F}$, the friction, and $\dot{\theta}$ the non-adiabatic heating rate. Equation (1) indicates that the PV is conserved in an adiabatic, frictionless closed system. Define the PV substance Π as:

$$\Pi = \rho PV = \vec{\xi_a}\cdot\nabla\theta, \quad (2)$$

PV is the amount of Π per unit air mass. Equation (1) can be simplified as:

$$\frac{\partial\Pi}{\partial t} = -\nabla\cdot\left(\vec{V}\Pi - \vec{\xi_a}\dot{\theta} - \vec{F}\times\nabla\theta\right), \quad (3)$$

Since PV is not conserved in the presence of diabatic processes, the PV tendency can be utilized to identify the contribution of non-conservation processes to the PV field, and then quantify the impact of these processes on the atmosphere via piecewise PV inversion. In a complete dynamic model, such as the WRF model, (3) is fully operational. However, in the ICAR model, due to the simplified dynamics, the PV tendency is not the same as in WRF because the physical processes like the diabatic heating do not interact with the winds.

$$\frac{\partial\Pi}{\partial t}_{ICAR} = -\nabla\cdot\left(\vec{V}\Pi - \vec{\xi_a}\dot{\theta} - \vec{F}\times\nabla\theta\right)_{ICAR}, \quad (4)$$

The differences on the right-hand side of (3) and (4) can help us comprehend the impact of the "physical–dynamical interactions" on the predictability of precipitation. Subtracting (4) from (3) and taking a volume integral,

$$\frac{\partial}{\partial t}\iiint(\Pi_{WRF}-\Pi_{ICAR})dv=-\iiint\nabla\cdot(\vec{V}\Pi-\overrightarrow{\xi_a}\dot{\theta}\ -\vec{F}\times\nabla\theta)_{WRF}-\nabla\cdot(\vec{V}\Pi-\overrightarrow{\xi_a}\dot{\theta}\ -\vec{F}\times\nabla\theta)_{ICAR}\,dv, \tag{5}$$

As in [41], the volume for (5) is made up of three distinct parts, two of which lie in isentropic surfaces (e.g., 330 K and 350 K or 350 K and 380 K), and a third lies between these isentropic surfaces and around a precipitation area of research interest (e.g., the red circle in Figure 9g). Using Gaussian formula, (5) can be written as:

$$\frac{\partial}{\partial t}\iiint(\Pi_{WRF}-\Pi_{ICAR})dv=\iint[(\vec{V}\Pi-\overrightarrow{\xi_a}\dot{\theta}\ -\vec{F}\times\nabla\theta)_{WRF}-(\vec{V}\Pi-\overrightarrow{\xi_a}\dot{\theta}\ -\vec{F}\times\nabla\theta)_{ICAR}]\cdot\boldsymbol{ds}, \tag{6}$$

Figure 10 depicts the PV (color-filled) and winds (wind vector) at 2 km, 5.5 km, and 8.5 km heights at 12 UTC on 20 July 2021. Compared with Figure 10d–f, Figure 10a–c shows that the PV in the ICAR model is smooth and exhibits coarse grain characteristics. In contrast, in Figure 10d–f, the PV from the WRF model exhibits intense small-scale PV bands corresponding to the moist convection. Figure 10g–i highlights the disparities in PV and wind fields between WRF and ICAR. Essentially, the PV difference between WRF and ICAR is related to the differences between the winds and potential temperature fields of the two models. Specifically, the fluctuations in the PV and wind fields over the plains region correspond to the small-scale convective systems generated by the "physical–dynamical interactions". When the lower isentropic surface is above the planetary boundary layer and over a short duration, the contribution of friction and PV flux at the lateral boundaries to PV tendency are relatively small, and the PV difference in the volume is mainly due to the diabatic heating at the upper and bottom boundaries. The latent heat release resulting from the condensation of water vapor typically peaks at mid-to-high levels. Therefore, the latent heat release modifies the vertical distribution of PV. The precipitation in Figure 9 and the PV disparities shown in Figure 10g–i qualitatively demonstrate the impact of latent heat release. In particular, the mean latent heat release above a large area of precipitation enhances (reduces) the PV below (above) the maximum condensation level. The shading in Figure 10j–l shows the disparities of vertical vorticity, which closely aligns with the PV disparities in Figure 10g–i. According to Stoke's theorem ($\oint\vec{V}\cdot\boldsymbol{dl}=\iint\vec{\xi}\cdot\boldsymbol{ds}$), the circulation of any closed loop (e.g., the red ellipses in Figure 10j–l is equal to the integral of the normal component of vorticity over the area enclosed by the closed loop (e.g., the red ellipses). Then, the cyclonic and anticyclonic circulations in Figure 10j–l are associated with the area integral of the vertical vorticity disparities (shadings), which is proportional to the PV disparities in Figure 10g–i. Actually, the wind differences derived by subtracting the winds of ICAR from those of WRF shown in Figure 10g–i and its streamlines shown in Figure 10j–l reveal that there are larger-scale cyclonic circulations in the lower- to mid-level of atmosphere and anticyclonic circulations in the upper atmosphere in areas with precipitation.

Corresponding to numerous convective-scale heavy rainfalls, there are several smaller but intense cyclonic/anticyclonic circulations within the area of larger-scale cyclonic/anticyclonic circulation in Figure 10j–l. With the Stoke's theorem, we know that the small-scale vorticity can impact the larger-scale circulation. That is why inaccuracies in convective-scale motions may lead to inaccuracies in large-scale winds. These results provide us with a basis to understand the predictability of severe precipitation and the connections between provincial-scale and convective-scale precipitation. We should mention that the vertical shear of horizontal winds and strong vertical motions may change the vertical distribution of vorticity on the convective scale. For example, Weijenborg et al. [51] discovered that vertical wind shear distorts the centers of small and intense positive/negative vorticity. However, in general, our discussion about the circulation is still correct.

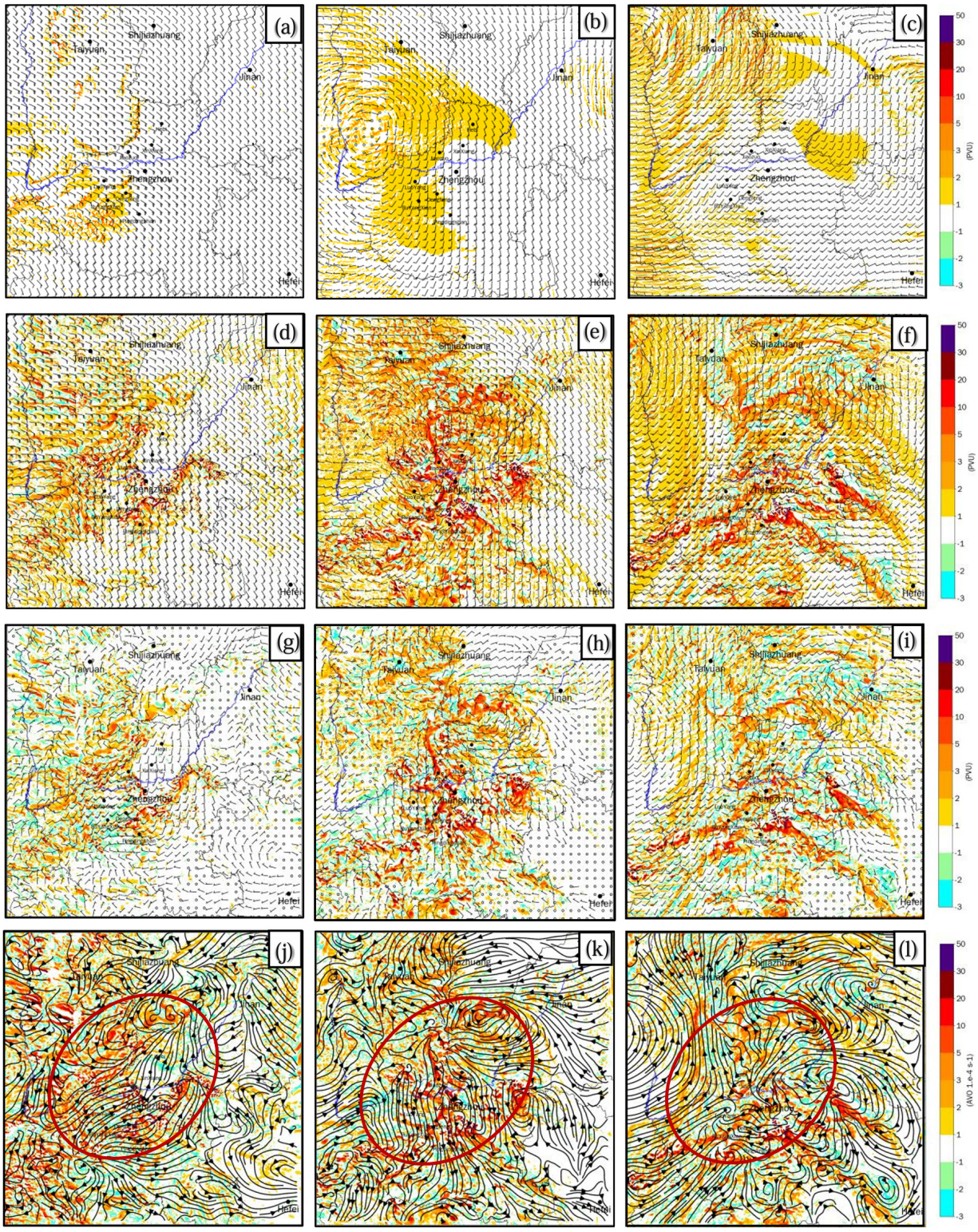


Figure 10. The PV field (color-filled) and winds (barbs) at 2 km, 5.5 km, and 8.5 km heights at 12 UTC on 20 July 2021, with the models starting at 00UTC on 19 July: (**a**–**c**) ICAR; (**d**–**f**) WRF; (**g**–**i**) are the disparities in PV and wind fields between WRF and ICAR; (**j**–**l**) are the disparities in absolute vorticity and streamlines of winds disparities between WRF and ICAR at 2 km, 5.5 km, and 8.5 km heights.

We have seen that severe precipitation is associated with a smaller-scale moist convection and possible impacts of the moist convection on a larger-scale flow. To understand the predictability of heavy rainfall and use the predictability to improve the forecast accuracy of heavy precipitation, let us refresh our knowledge about the predictability first. The intrinsic predictability and the initial error growth at different scales have been thoroughly investigated [52–56]. The predictability of the atmosphere at the convective scale is different from that at the synoptic scale. Many studies (e.g., [57–60]) have underlined the importance of convective instability in disrupting mesoscale predictability. Other than intrinsic predictability, practical predictability refers to the "ability to predict based on the procedures currently available" [61,62]. The practical predictability of atmospheric motions with different scales has been investigated using various numerical models. Walser et al. [63] pointed out that the uncertainties in precipitation forecasts increase rapidly with decreasing scale as individual convective cells are rendered unpredictable by chaotic aspects of the moist dynamics. Wang et al. [64] investigated the predictability of heavy precipitation through a series of convection-permitting simulations of three cases in different synoptic backgrounds. They found that heavier precipitation has larger uncertainty or less predictability. More recently, Zhu et al. [65] studied the predictability of the Henan 21.7 Rainstorm through ensemble forecasts of two sets of convective discernible scales. They found that most members had position biases in the extreme precipitation near Zhengzhou. For the extreme hourly rainfall, the position error ranged from tens to hundreds of kilometers. Zhang et al. [66] conducted convection-resolvable ensemble simulations of the Henan 21.7 Rainstorm using the WRF model. They found that errors in moist convection activity can increase the error growth rates at all scales, especially at small scales. Their findings are consistent with the error growth model of Zhang et al. [67]. Selz and Craig [68] pointed out that while the initial growth was mainly in the divergent part of the flow, the eventual slow growth on large scales was more in the rotational component. Hohenegger et al. [69,70] illustrated that the error growth rates are around 10 times larger and the tangent linear approximation breaks down within a couple of hours. They thought that rapid loss of linearity implies a fundamental qualitative difference between convective-scale and synoptic-scale forecasting. Poor convective-scale predictability is most likely due to the significant nonlinearities of the atmosphere at smaller scales: microphysics, turbulence, radiation, and flow dynamics are strongly coupled and can act to amplify both model and observation uncertainties.

While the predictability of severe precipitation is limited by the rapid error growth dominated by the nonlinear moist processes in it, the background forcing can increase the predictability of small-scale convection. Done et al. [71] and Flack et al. [72] showed that convection in "non-equilibrium" convective conditions [73], that is under the influence of fronts and other localized synoptic features, exhibited better predictability than convection in "quasi-equilibrium" conditions with a fairly uniform large-scale environment. Surcel et al. [74] showed that diurnally forced convection under weak synoptic forcing exhibited lower predictability and higher sensitivity to initial conditions than widespread convection under strong synoptic forcing. Following these results, the terrain as a fixed geographical forcing characteristic should increase the predictability of severe precipitation. For example, mountain topography could decrease the degree of freedom of the atmosphere by providing a stationary, steady-state forcing [20]. However, the study about the impact of topography on the convective scale predictability is still limited. Bachmann et al. [75,76] demonstrated in an idealized setup that orographic forcing alters the likelihood of convection occurrence in its vicinity where both lower and higher probabilities of convection enhance predictability at a particular location. Wu and Takemi [77,78] conducted identical twin experiments with and without topography in an idealized framework to investigate the impact of topography on the initial error growth associated with moist convection. They found that moist convection develops and organizes into a larger size in the experiment with topography. Their analysis based on individual cloud areas shows that the convective clouds developing over the mountain have less error growth at the early stage of development. The studies

indicated that orography reduces displacement errors nearby and, consequently, enhances the predictability of convective precipitation.

To summarize the discussion: the larger-scale systems have a longer predictable time (higher predictability), while the smaller-scale systems have a shorter predictable time (lower predictability). Due to the uncertainty in initial conditions, deficiencies in model physics, and inaccurate empirical parameters describing convective processes in the model, the predictability of moist convection is generally low. The moist convective systems are more predictable in a strong forcing environment than in a weak forcing environment. This research focuses on the prediction of severe precipitation. We decompose the precipitation according to its formation mechanism and the effects of orographic forcing and the "physical–dynamical interactions" on the practical predictability. At first, the WRF's forecast is divided into a slowly varying larger-scale background field and a rapidly varying small-to-medium-scale residual. In this study, we use the forecast of the coarse-resolution WRF model as the background field. The spatiotemporal variation of the background field is relatively slow (e.g., Figure 10a–c). Meanwhile, the spatiotemporal variation of residual dominated by the small-to-medium-scale systems is rapid (e.g., Figure 10g–i). The residual can be further decomposed into a "terrain-forced component" and a "non-terrain-forced component". The disparities between WRF and ICAR are due to the "physical–dynamic interactions". Though the "physical–dynamical interactions" also influence the "terrain-forced component", e.g., the orographic precipitation, our previous analysis indicates that the nonlinear interactions between the terrain-forced component and the small-scale flow are relatively weak. Therefore, the "terrain-forced component" is primarily generated by the forcing of smaller-scale terrain (such as mountains, valleys, etc.) on the smooth background field. Since ICAR's forecast is composed of a "terrain-forced component" and a weak background forcing component, the "terrain-forced component" of ICAR approximately represents the "terrain-forced component" of WRF. Meanwhile, the "non-terrain-forced component" beyond terrain can be approximated by the disparities between WRF and ICAR, and the "non-terrain-forced component" beyond terrain is mostly generated by the "physical–dynamical interactions". For instance, the small eddies beyond the terrain in Figure 10j–l are the "non-terrain-forced component". With this decomposition and the common understanding of predictability, we know that the predictability of severe small-scale orographic precipitation should be relatively high because it is generated by the forcing of settled orography on the larger-scale background field. On the other hand, the predictability of severe non-orographic precipitation is relatively low because the moist convection in a weak forcing environment is generally less predictable. Knowing that severe orographic precipitation is more predictable than severe non-orographic precipitation, the concern is whether we can improve precipitation forecasts through the predictability of various severe rainfalls, e.g., by giving more weight to severe orographic precipitation and less weight to severe non-orographic precipitation.

4.3. Quantitative Evaluation of Rainfall Forecasting and Accuracy Improvement

The CHM_PRE dataset [26,27] effectively represents the spatiotemporal distribution of actual precipitation. Hence, CHM_PRE is utilized for the quantitative assessment of precipitation forecasts. Following procedures used for other case studies [64,79,80], a quantitative evaluation of precipitation is carried out for four 72 h forecasts from 00 UTC on 17 July 2021, to 00 UTC on 20 July 2021, at 24 h intervals. The skill scores of BS, TS, FAR, and POD within the geographical range of 111–118° E, 32–38° N are computed with CHM_PRE as observations. The definitions of BS, TS, FAR, and POD and the Contingency Table A1 are in Appendix A. Figure 11 illustrates BS, TS, FAR, and POD of the 0–24 h, 24–48 h, and 48–72 h accumulative precipitation forecasts for the Henan 21.7 Rainstorm event. The scores suggest that the precipitation forecast skill for 24–48 h is superior to that for 0–24 h and 48–72 h because the initial field is downscaled solely from the NCEP GFS forecast without data assimilation. This outcome aligns with the typical error patterns in numerical weather prediction: (1) a larger forecast error is observed during the model

spin-up phase, (2) the error decreases to its minimum after the spin-up, and (3) as the forecast progresses, the error grows with the forecast lead time. Figure 11 illustrates that for the 24–48 h cumulative precipitation, the WRF model outperforms the ICAR model in TS and POD scores but exhibits over-forecast (BS > 1) and a larger false alarm rate (FAR). When daily precipitation exceeds 200 mm, the skill scores of WRF and ICAR are closer. For 0–24 h and 48–72 h daily accumulative precipitation, the conclusions are similar. The direct comparison of precipitation forecasts with CHM_PRE depicted in Figure 8 aligns with this quantitative evaluation. From the perspective of precipitation forecasting skill scores for both models, the WRF model exhibits higher accuracy than the ICAR model. However, the "physical–dynamical interactions" within the WRF model can lead to larger errors in convective precipitation as the rainfall intensity increases. In contrast, the ICAR model effectively reflects the key mechanism of heavy precipitation induced by topographic forcing in the mountainous regions. Consequently, the error associated with intensive precipitation remains relatively minor, thereby partially compensating for the shortcomings of the WRF model. We can explain the skill differences through the vorticity and circulation shown in Figure 10g–l. Since the WRF model considers the impacts of precipitation physics on the winds, the mesoscale circulation caused by mesoscale precipitation (e.g., the area with daily precipitation exceeding 5 mm) can be depicted. In the meantime, the mesoscale circulation caused by mesoscale precipitation is neglected in the ICAR model. Therefore, the skill scores of WRF are higher than ICAR when daily precipitation is less than 100 mm. The skill scores of ICAR and WRF start to converge as the precipitation intensity exceeds 100 mm. This fact again highlights the difference in predictability between severe orographic and non-orographic precipitation. Previous analysis shows that severe non-orographic precipitation caused by small-scale moist convection is associated with the "physical–dynamical interactions" in the WRF model. It is difficult to predict the moist convection in a weak forcing environment in terms of timing and spatial distribution (e.g., Figure 8b vs. Figure 8e). In contrast, the ICAR model filters out these poorly predictable processes linked to the "physical–dynamical interactions" while keeping the more predictable processes related to the topographic forcing on the larger-scale airflow, which dominates the severe orographic precipitation. The skill scores of ICAR decrease more slowly as rainfall intensity increases.

Knowing that severe orographic precipitation is more predictable than severe non-orographic precipitation, we can give more weight to severe orographic precipitation and less weight to severe non-orographic precipitation. As a trial, we take an arithmetic mean of precipitation on grid points where ICAR predicts daily precipitation exceeding 100 mm and WRF predicts daily precipitation less than 100 mm. This adjustment increases the weight of severe orographic precipitation. Also, we take an arithmetic mean of grid point daily precipitation where ICAR predicts less than 15 mm and WRF predicts more than 100 mm to decrease the weight of severe non-orographic precipitation. Meanwhile, we continue to use the WRF's precipitation forecast for other grid points. As shown by the dashed line in Figure 10, the skill scores of precipitation forecasts are indeed improved.

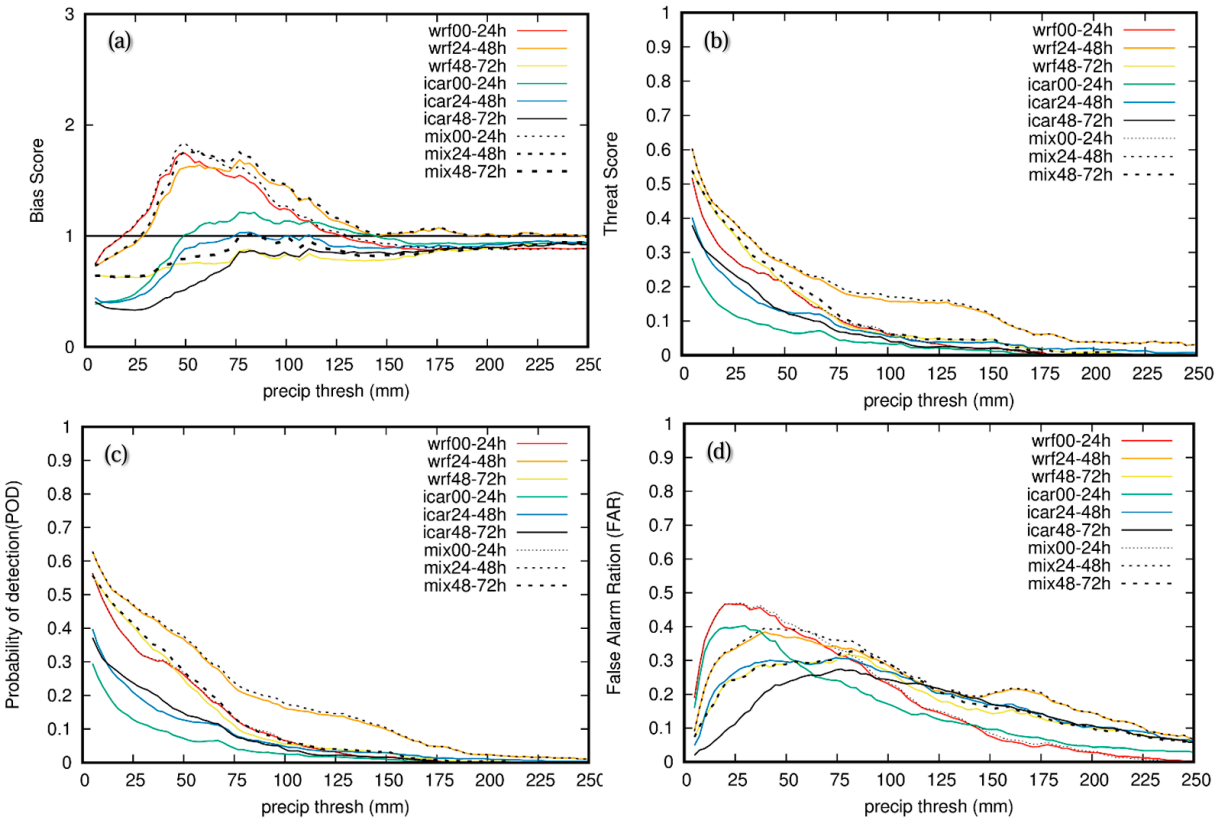


Figure 11. The scores of (**a**) BIAS, (**b**) TS, (**c**) POD, and (**d**) FAR of the accumulative precipitation for the four 72 h forecasts initialized at 00 UTC on 17, 18, 19, and 20 July 2021. The red, orange, and yellow colors represent the scores of the 1-, 2-, and 3-day forecasts from WRF, while the green, blue, and black colors present the scores of the 1-, 2-, and 3-day forecasts from ICAR. The black dotted and dashed lines represent the scores of the adjusted precipitation forecasts.

5. Discussion

Heavy precipitation events often challenge agriculture, infrastructure, and public safety. Timely and precise predictions of heavy precipitation enable authorities to implement necessary measures, thereby mitigating potential harm to individuals and minimizing property damage. Therefore, heavy precipitation forecasting is integral to disaster preparedness, agricultural management, and economic stability. By enhancing our ability to predict and respond to heavy precipitation, societies can significantly mitigate the risks associated with extreme weather, safeguarding lives, livelihoods, and infrastructure.

Previous studies have shown that orography plays a significant role in triggering and organizing the moist convection responsible for the formation of severe orographic rainfall. However, more in-depth studies are needed to reveal the complicated mechanisms of severe orographic precipitation. How do the complex terrain and associated dynamical and physical processes affect the intensity and location of precipitation? Can we use the predictabilities caused by various factors to improve the accuracy of precipitation forecasts? It is hard to answer these questions just by diagnosing the results from a single numerical model because the effects of various processes on precipitation are mixed. Conducting ensemble sensitivity experiments with a dynamic model may answer these questions. However, the huge computational cost of high-resolution ensemble sensitivity experiments makes it impracticable in a workplace with limited computational resources. In addition, extracting conclusive information from a large volume of complex data is another intricate task. In contrast, using atmospheric models with different complexities of dynamics to simulate the same weather event can easily provide answers to these questions. This article

provides an example by conducting re-forecast experiments on the Henan 21.7 Rainstorm using a simplified dynamics model (ICAR) and a complete dynamics model (WRF).

Since the WRF model has considered the impacts of precipitation physics on the winds, the mesoscale circulation caused by mesoscale precipitation (e.g., the area with daily precipitation exceeding 5 mm) can be depicted. ICAR ignores the impact of physical processes on the winds. Therefore, the mesoscale circulation caused by mesoscale precipitation cannot be considered in ICAR. That is the reason why WRF's skills are higher than the ICAR model's when precipitation is weak. On the other hand, due to large uncertainty (error) in the small-scale moist convection in the weak forcing environment, the forecasting skills for severe non-orographic precipitation are much lower than for severe orographic precipitation. The fact that the forecasting skills of ICAR do not rapidly decrease with increasing intensity indicates that ICAR captures the key factor for the generation of severe orographic precipitation. The key factor is the forcing of high-resolution topography on the smooth background airflow, which has better predictability.

Based on the fact that ICAR has good skill in predicting severe orographic precipitation, we proposed a precipitation forecast scheme to improve the skill of precipitation forecasts by giving more weight to severe orographic precipitation and less weight to severe non-orographic precipitation. When severe precipitation occurs near orography in the ICAR model, we think that the severe precipitation occurs there. Conversely, when the severe precipitation in the WRF model occurs beyond the orography, the severe precipitation is unlikely to be there. As an initial prototype, we take an arithmetic mean of precipitation on grid points where ICAR predicts daily precipitation exceeding 100 mm and WRF predicts daily precipitation of less than 100 mm. Meanwhile, we take an arithmetic mean of daily precipitation on grid points where ICAR's prediction is less than 15 mm and WRF's prediction is more than 100 mm. The precipitation on other grid points is unchanged. These weighting methods increase (decrease) the points of severe orographic (non-orographic) precipitation. The good thing is the adjustment has improved the quantitative precipitation prediction.

Despite the apparent improvement in this prototype's ability to forecast severe orographic precipitation, the prototype should be cautiously accepted. We should remember the necessity of further investigation across multiple cases to substantiate its validity and enhance its robustness in practical applications. We will test this approach with more events, particularly extreme events, to demonstrate its reliability. In essence, the richness of a single case event should be integrated within a broader framework of inquiry to truly capture the nuances and variances inherent in the severe orographic precipitation. In addition, the "impacts of physical processes on winds and the nonlinear interactions between the small resolvable-scale disturbances" on precipitation is a synthetic effect of winds, cloud physics, and topography profiles. More diagnoses are needed to get specific information about the actions of each component.

As a prototype for adjustment of WRF's precipitation forecasts in this study, we intuitively use a simple arithmetic mean of the two models' precipitations of different predictability. More sophisticated approaches can be used to modify the precipitation forecast of WRF with ICAR's precipitation forecast. The forecast accuracy can be further improved with a better adjustment method. In the future, we will collect high-resolution automatic weather station data to evaluate our forecasts and conduct more case studies using the same procedure.

6. Conclusions

The Intermediate Complexity Atmospheric Research Model (ICAR) and the Weather Research and Forecasting Model (WRF) with a 1 km horizontal grid spacing are used for the re-forecasts for the Henan 21.7 Rainstorm. The forecast differences between WRF and ICAR are due to the presence/absence of the "physical–dynamical interactions".

The severe precipitation in ICAR is primarily due to the uplifting of terrain against relatively gentle background airflow. Thus, heavy precipitation forecasted by ICAR primarily

accumulates on the windward slopes of the mountains, and the location of the orographic precipitation in ICAR varies slowly over time. The non-orographic precipitation of ICAR is much weaker than that of WRF.

The orographic precipitation of WRF corresponds well with the orographic precipitation of ICAR. In addition the severe orographic precipitation, some severe precipitation forecasted by WRF is beyond the mountains. The heavy precipitation beyond the mountains is attributed to the "physical–dynamical interactions". The coincidence of severe precipitation and vertical velocity indicates that severe non-orographic precipitation in WRF is associated with moist convection. Due to the uncertainty in initial conditions, deficiencies in model physics, and inaccurate empirical parameters describing convective processes in the complete dynamical model, the predictability of moist convective systems is generally low in a weak forcing environment. Therefore, the severe non-orographic precipitation forecasted by WRF has little correspondence with the observations.

The severe precipitation on the windward slopes of the mountains typically aligns with the observations, whereas the heavy rainfall beyond the mountains seldom matches the observations. Therefore, the severe precipitation on the windward slopes of (beyond) the mountains is more (less) predictable. The quantitative evaluation of the precipitation forecasts of the two models demonstrates the following. The forecasting skills of the WRF model are higher than the ICAR model when precipitation is weak (daily precipitation less than 100 mm). For severe precipitation (daily precipitation exceeding 100 mm), the forecasting skills of the two models are close. Based on these findings and theoretical thinking about the predictability of severe precipitation, a scheme of using ICAR's prediction to adjust WRF's prediction is proposed, thereby improving the forecast accuracy of heavy rainfall.

Supplementary Materials: The following supporting information can be downloaded at: https://www.mdpi.com/article/10.3390/atmos15080959/s1, Figure S1: Accumulative precipitation of seven reforecasts.

Author Contributions: Conceptualization, X.W.; methodology, X.W., Q.X. and X.D.; formal analysis, X.W., H.Z. and Q.T.; data curation, X.D. and F.Q.; project administration, T.Z. and W.P.; writing—original draft preparation, X.W.; writing—review and editing, Q.X., X.D., H.Z., Q.T. and T.Z.; visualization, X.W.; funding acquisition W.P. All authors have read and agreed to the published version of the manuscript.

Funding: This research received no external funding.

Institutional Review Board Statement: Not Applicable.

Informed Consent Statement: Not Applicable.

Data Availability Statement: The precipitation dataset for Chinese Mainland (CHM_PRE) is publicly available from https://doi.org/10.11888/Atmos.tpdc.300523. The raw data supporting the investigations of this article are available on request. The data are not publicly available due to file sizes.

Acknowledgments: The authors acknowledge the helpful reviews and constructive comments by the editor and anonymous reviewers that significantly improved the manuscript. We thank the NCAR for making the WRF and ICAR models publicly available. This article is part of the research developed under the Numerical Weather Forecasting Project of the Newsky Technology Co., Ltd., titled "Aerospace New Meteorological Numerical Analysis and Prediction System (AN-DAPS)." This research would not have been possible without the computing and human resources provided by the company. We are sincerely grateful for the company's support.

Conflicts of Interest: Authors Xingbao Wang, Qun Xu, Xiajun Deng, Hongjie Zhang, Qianhong Tang, Tingting Zhou, Fengcai Qi and Wenwu Peng were employed by the company Newsky Technology Co., Ltd. The remaining author declares that the research was conducted in the absence of any commercial or financial relationships that could be construed as a potential conflict of interest.

Appendix A Definitions of BS, TS, POD and FAR

Table A1. Contingency table [80].

	Observation YES	Observation NO
Forecast YES	*a*	*b*
Forecast NO	*c*	*d*

$$BS = \frac{a+b}{a+c}$$

$$TS = \frac{a}{(a+b+c)}$$

$$POD = \frac{a}{a+c}$$

$$FAR = \frac{b}{a+b}$$

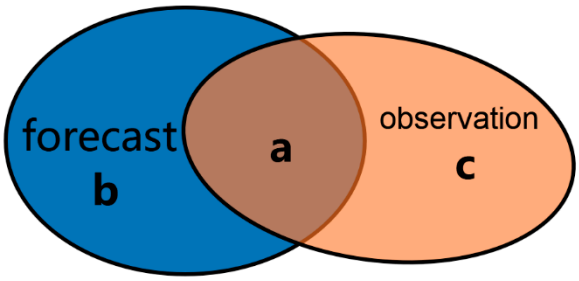


Figure A1. Classification of Forecast and Observation.

BS: A measure of precipitation frequency forecast, BS = 1 perfect, BS > 1 over-forecast, BS < 1 under-forecast. TS: A measure of precipitation forecast accuracy, TS = 1 perfect, TS = 0 no forecasting skill. POD: Probability of detection for precipitation forecast, POD = 1 perfect, POD = 0 no forecasting skill (similar to TS). FAR: False alarm rate for precipitation forecast, FAR = 0 perfect, FAR = 1 no forecasting skill. A single index cannot fully reflect the skill of precipitation forecasting, several indices must be used in combination to roughly estimate the quality of precipitation forecasts.

References

1. Liang, X.; Xia, R.; Bao, X.; Zhang, X.; Wang, X.; Su, A.; Fu, J.; Li, H.; Wu, C.; Yu, M.; et al. Preliminary investigation on the extreme rainfall event during July 2021 in Henan Province and its multi-scale processes. *Chin. Sci. Bull.* **2022**, *67*, 997–1011. (In Chinese) [CrossRef]
2. Su, A.; Lu, X.; Cui, L.; Li, Z.; Xi, L.; Li, H. The basic observational analysis of "7.20" Extreme Rainstorm in Zhengzhou. *Torrential Rain Disasters* **2021**, *40*, 445–454. (In Chinese)
3. Chyi, D.; He, L.; Wang, X.; Chen, S. Fine observation characteristics and thermodynamic mechanisms of extreme heavy rainfall in Henan on 20 July 2021. *J. Appl. Meteorol. Sci.* **2022**, *33*, 1–15. (In Chinese) [CrossRef]
4. Zhang, X.; Yang, H.; Wang, X.; Shen, L.; Wang, D.; Li, H. Analysis on characteristic and abnormality of atmospheric circulations of the July 2021 extreme precipitation in Henan. *Trans. Atmos. Sci.* **2021**, *44*, 672–687. (In Chinese) [CrossRef]
5. Sun, J.; Fu, S.; Wang, H.; Zhang, Y.; Chen, Y.; Su, A.; Wang, Y.; Tang, H.; Ma, R. Primary characteristics of the extreme heavy rainfall event over Henan in July 2021. *Atmos. Sci. Lett.* **2022**, *24*, e1131. [CrossRef]
6. Yin, L.; Ping, F.; Mao, J.; Jin, S. Analysis on Precipitation Efficiency of the "21.7" Henan Extremely Heavy Rainfall Event. *Adv. Atmos. Sci.* **2023**, *40*, 374–392. [CrossRef]
7. Hsu, P.-C.; Xie, J.; Lee, J.; Zhu, Z.; Li, Y.; Chen, B.; Zhang, S. Multiscale interactions driving the devastating floods in Henan Province, China during July 2021. *Weather Clim. Extrem.* **2023**, *39*, 100541. [CrossRef]
8. Tran, T.-N.-D.; Le, M.H.; Zhang, R.; Nguyen, B.Q.; Bolten, J.D.; Lakshmi, V. Robustness of gridded precipitation products for Vietnam basins using the comprehensive assessment framework of rainfall. *Atmos. Res.* **2023**, *293*, 106923. [CrossRef]

9. Aryal, A.; Tran, T.-N.-D.; Kumar, B.; Lakshmi, V. Evaluation of Satellite-Derived Precipitation Products for Streamflow Simulation of a Mountainous Himalayan Watershed: A Study of Myagdi Khola in Kali Gandaki Basin, Nepal. *Remote Sens.* **2023**, *15*, 4762. [CrossRef]
10. Tao, S. *Torrential Rain in China*; Science Press: Beijing, China, 1980; pp. 1–225. (In Chinese)
11. Ding, Y.; Cai, Z.; Li, J. A case study on the excessively severe rainstorm in Henan province in early August 1975. *Chin. J. Atmos. Sci.* **1978**, *2*, 276–289. (In Chinese)
12. Chen, M.; Fu, B.; Yu, Q. Influence of topography on storm rainfall. *Acta Geogr. Sin.* **1995**, *50*, 256–263. (In Chinese)
13. Sun, J. The effects of vertical distribution of the lower-level flow on precipitation location. *Plateau Meteorol.* **2005**, *24*, 62–69. (In Chinese)
14. Chen, M.; Wang, Y.; Xiao, X.; Gao, F. Initiation and propagation mechanism for the Beijing extreme heavy rainstorm clusters on 2l July 2012. *Acta Meteorol. Sin.* **2013**, *71*, 569–592. (In Chinese)
15. Wang, C.; Yu, X.; Li, Z.; Li, J.; Wang, X. Investigation of extreme flash-rain events on the impact of Taihang Mountain. *Meteorol. Mon.* **2017**, *43*, 425–433. (In Chinese)
16. Wang, L.; Miao, J.; Han, F. Overview of impact of topography on precipitation in China over last 10 years. *Meteorol. Sci. Technol.* **2018**, *46*, 64–75. (In Chinese)
17. Zhong, S. Advances in the study of the influencing mechanism and forecast methods for orographic precipitation. *Plateau Meteorol.* **2020**, *39*, 1122–1132. (In Chinese) [CrossRef]
18. Smith, R.B. The influence of mountains on the atmosphere. *Adv. Geosci.* **1979**, *6*, 77–81.
19. Smith, R.B. Progress on the theory of orographic precipitation. In *Tectonics, Climate, and Landscape Evolution: Geological Society of America Special Paper 398*; Penrose Conference Series; Willett, S.D., Hovius, N., Brandon, M.T., Fisher, D.M., Eds.; The Geological Society of America: Boulder, CO, USA, 2006; pp. 1–16. [CrossRef]
20. Houze, R.A. Orographic effects on precipitating clouds. *Rev. Geophys.* **2012**, *50*, RG1001. [CrossRef]
21. Tran, T.-N.-D.; Nguyen, B.Q.; Zhang, R.; Aryal, A.; Grodzka-Łukaszewska, M.; Sinicyn, G.; Lakshmi, V. Quantification of Gridded Precipitation Products for the Streamflow Simulation on the Mekong River Basin Using Rainfall Assessment Framework: A Case Study for the Srepok River Subbasin, Central Highland Vietnam. *Remote Sens.* **2023**, *15*, 1030. [CrossRef]
22. Zhang, Y.; Sun, J.; Fu, S.; Wang, H.; Fu, Y.; Tang, H.; Wei, Q. Active Characteristics of Mesoscale Systems during the Heavy Rainfall in Henan Province in July 2021. *Chin. J. Atmos. Sci.* **2023**, *47*, 1196–1216. (In Chinese) [CrossRef]
23. Wei, P.; Xu, X.; Xue, M.; Zhang, C.; Wang, Y.; Zhao, K.; Zhou, A.; Zhang, S.; Zhu, K. On key dynamical processes supporting the 21·7 Zhengzhou record-breaking hourly rainfall in China. *Adv. Atmos. Sci.* **2022**, *40*, 337–349. [CrossRef]
24. Gutmann, E.D.; Barstad, I.; Clark, M.P.; Arnold, J.R.; Rasmussen, R.M. The Intermediate Complexity Atmospheric Research Model (ICAR). *J. Hydrometeorol.* **2016**, *17*, 957–973. [CrossRef]
25. Skamarock, W.C.; Klemp, J.B.; Dudhia, J.; Gill, D.O.; Barker, D.M.; Duda, M.G.; Huang, X.-Y.; Wang, W.; Powers, J.G. *A Description of the Advanced Research WRF Version 3*; NCAR Technical Note NCAR/TN-475+STR; NCAR: Boulder, CO, USA, 2008; 113p. [CrossRef]
26. Miao, C.; Han, J.; Guo, J. *The Daily Precipitation Dataset of China (1961–2022, 0.1°/0.25°/0.5°)*; National Tibetan Plateau Data Center: Beijing, China, 2023. (In Chinese) [CrossRef]
27. Han, J.; Miao, C.; Gou, J.; Zheng, H.; Zhang, Q.; Guo, X. A new daily gridded precipitation dataset for the Chinese mainland based on gauge observations. *Earth Syst. Sci. Data* **2023**, *15*, 3147–3161. [CrossRef]
28. Uuemaa, E.; Ahi, S.; Montibeller, B.; Muru, M.; Kmoch, A. Vertical accuracy of freely available global digital. *Remote Sens.* **2020**, *12*, 3482. [CrossRef]
29. Lakshmi, S.E.; Yarrakula, K. Review and critical analysis on digital elevation models. *Geofizika* **2019**, *35*, 129–157. [CrossRef]
30. Tran, T.-N.; Nguyen, B.Q.; Vo, N.D.; Le, M.-H.; Nguyen, Q.-D.; Lakshmi, V.; Bolten, J.D. Quantification of global Digital Elevation Model (DEM)—A case study of the newly released NASADEM for a river basin in Central Vietnam. *J. Hydrol. Reg. Stud.* **2023**, *45*, 101282. [CrossRef]
31. Wang, X.; Cui, C.; Wang, J.; Yang, J.; Zhou, W. Diagnostic analysis on water vapor and jet characteristics of the July 2021 severe torrential rain in Henan Province. *Meteorol. Mon.* **2022**, *48*, 533–544. (In Chinese)
32. Kain, J.S. The Kain-Fritsch convective parameterization: An update. *J. Appl. Meteorol.* **2004**, *43*, 170–181. [CrossRef]
33. Thompson, G.; Rasmussen, R.M.; Manning, K. Explicit forecasts of winter precipitation using an improved bulk microphysics scheme. *Part I Descr. Sensit. Anal. Mon. Weather Rev.* **2004**, *132*, 519–542. [CrossRef]
34. Thompson, G.; Field, P.R.; Rasmussen, R.M.; Hall, W.D. Explicit Forecasts of Winter Precipitation Using an Improved Bulk Microphysics Scheme. Part II: Implementation of a New Snow Parameterization. *Mon. Weather Rev.* **2008**, *136*, 5095–5115. [CrossRef]
35. Thompson, G.; Eidhammer, T. A study of aerosol impacts on clouds and precipitation development in a large winter cyclone. *J. Atmos. Sci.* **2014**, *71*, 3636–3658. [CrossRef]
36. Grell, G.; Dudhia, J.; Stauffer, D. *A Description of the Fifth-Generation Penn State/NCAR Mesoscale Model (MM5)*; NCAR Technical Note NCAR/TN-398 + STR; NCAR: Boulder, CO, USA, 1994; p. 117.
37. Dudhia, J. A multilayer soil temperature model for MM5. In Proceedings of the Sixth PSU/NCAR Mesoscale Model Users' Workshop, Boulder, CO, USA, 22–24 July 1996; pp. 49–50.

38. Dudhia, J.; Gill, D.; Manning, K.; Wang, W.; Bruyere, C. *PSU/NCAR Mesoscale Modeling System Tutorial Class Notes and User's Guide: Mm5 Modelling System Version 3*; PSU/NCAR: Boulder, CO, USA, 2004; p. 390.
39. Jimenez, P.A.; Dudhia, J.; Gonzalez-Ruoco, J.F.; Navarro, J.; Montavez, J.P.; Garcia-Bustamente, E. A revised scheme for the WRF surface layer formulation. *Mon. Weather Rev.* **2012**, *140*, 898–918. [CrossRef]
40. Hong, S.-Y.; Noh, Y.; Dudhia, J. A new vertical diffusion package with an explicit treatment of entrainment processes. *Mon. Weather Rev.* **2006**, *134*, 2318–2341. [CrossRef]
41. Iacono, M.J.; Delamere, J.S.; Mlawer, E.J.; Shephard, M.W.; Clough, S.A.; Collins, W.D. Radiative forcing by long-lived greenhouse gases: Calculations with the AER radiative transfer models. *J. Geophys. Res.* **2008**, *113*, D13103. [CrossRef]
42. Ding, Y. On the study of the unprecedented heavy rainfall in Henan Province during 4–8 August 1975: Review and assessment. *Acta Meteorol. Sin.* **2015**, *73*, 411–424. (In Chinese) [CrossRef]
43. Sun, J.; Chen, Y.; Yang, S.; Dai, K.; Chen, T.; Yao, R.; Xu, J. Analysis and thinking on the extremes of the 2l July 2012 torrential rain in Beijing Part I: Preliminary causation analysis and thinking. *Meteorol. Mon.* **2012**, *38*, 1267–1277. (In Chinese)
44. Xu, J.; Yang, S.; Sun, J.; Zhang, F.; Chen, Y. Discussion on the formation of a warm sector torrential rain case in North China. *Meteorol. Mon.* **2014**, *40*, 1455–1463. (In Chinese)
45. Ran, L.; Li, S.; Zhou, Y.; Yang, S.; Ma, S.; Zhou, K.; Shen, D.; Jiao, B.; Li, N. Observational analysis of the dynamic, thermal, and water vapor characteristics of the "7.20" extreme rainstorm event in Henan Province, 2021. *Chin. J. Atmos. Sci.* **2021**, *45*, 1366–1383. (In Chinese) [CrossRef]
46. Bueh, C.; Zhuge, A.; Xie, Z.; Gao, C.; Lin, D. Water vapor transportation features and key synoptic-scale systems of the "7.20" rainstorm in Henan Province. *Chin. J. Atmos. Sci.* **2022**, *46*, 725–744. (In Chinese) [CrossRef]
47. Ertel, H. Ein neuer hydrodynamische wirbdsatz. *Meteorol. Z. Braunschw.* **1942**, *59*, 277–281.
48. Hoskins, B.J.; McIntyre, M.E.; Robertson, A.W. On the use and significance of isentropic potential vorticity maps. *Q. J. R. Meteorol. Soc.* **1985**, *111*, 877–946. [CrossRef]
49. Haynes, P.H.; McIntyre, M.E. On the evolution of vorticity and potential vorticity in the presence of diabatic heating and frictional or other forces. *J. Atmos. Sci.* **1987**, *44*, 828–841. [CrossRef]
50. Li, H.; Wang, X.; Zhang, X.; Lü, L.; Xu, W. Analysis on extremity and characteristics of the 19 July 2016 severe torrential rain in the north of Henan Province. *Meteorol. Mon.* **2018**, *44*, 1136–1147. (In Chinese) [CrossRef]
51. Weijenborg, C.; Friederichs, P.; Hense, A. Organisation of potential vorticity on the mesoscale during deep moist convection. *Tellus A* **2015**, *67*, 25705. [CrossRef]
52. Lorenz, E.N. The predictability of a flow which possesses many scales of motion. *Tellus* **1969**, *21*, 289–307. [CrossRef]
53. Rotunno, R.; Snyder, C. A generalization of Lorenz's model for the predictability of flows with many scales of motion. *J. Atmos. Sci.* **2008**, *65*, 1063–1076. [CrossRef]
54. Sun, Y.Q.; Zhang, F. Intrinsic versus practical limits of atmospheric predictability and the significance of the butterfly effect. *J. Atmos. Sci.* **2016**, *73*, 1419–1438. [CrossRef]
55. Weyn, J.A.; Durran, D.R. The dependence of the predictability of mesoscale convective systems on the horizontal scale and amplitude of initial errors in idealized simulations. *J. Atmos. Sci.* **2017**, *74*, 2191–2210. [CrossRef]
56. Judt, F. Insights into atmospheric predictability through lobal convection-permitting model simulations. *J. Atmos. Sci.* **2018**, *75*, 1477–1497. [CrossRef]
57. Zhang, F.; Snyder, C.; Rotunno, R. Effects of moist convection on mesoscale predictability. *J. Atmos. Sci.* **2003**, *60*, 1173–1185. [CrossRef]
58. Zhang, F.; Bei, N.; Epifanio, C.C.; Rotunno, R.; Snyder, C. A multistage error-growth conceptual model for mesoscale predictability. *Bull. Amer. Meteorol. Soc.* **2006**, *87*, 287–288.
59. Zhang, F.; Odins, A.M.; Nielsen-Gammon, J.W. Mesoscale predictability of an extreme warm-season precipitation event. *Weather Forecast.* **2006**, *21*, 149–166. [CrossRef]
60. Hohenegger, C.; Lüthi, D.; Schär, C. Predictability mysteries in cloud-resolving models. *Mon. Weather Rev.* **2006**, *134*, 2095–2107. [CrossRef]
61. Lorenz, E.N. Atmospheric predictability as revealed by naturally occurring analogues. *J. Atmos. Sci.* **1969**, *26*, 636–646. [CrossRef]
62. Melhauser, C.; Zhang, F. Practical and intrinsic predictability of severe and convective weather at the mesoscales. *J. Atmos. Sci.* **2012**, *69*, 3350–3371. [CrossRef]
63. Walser, A.; Lüthi, D.; Schär, C. Predictability of precipitation in a cloud-resolving model. *Mon. Weather Rev.* **2004**, *132*, 560–577. [CrossRef]
64. Wang, X.; Steinle, P.; Seed, A.; Xiao, Y. The Sensitivity of Heavy Precipitation to Horizontal Resolution, Domain Size, and Rain Rate Assimilation: Case Studies with a Convection-Permitting Model. *Adv. Meteorol.* **2016**, *2016*, 7943845. [CrossRef]
65. Zhu, K.; Zhang, C.; Xue, M.; Yang, N. Predictability and skill of convection-permitting ensemble forecast systems in predicting the record-breaking "21·7" extreme rainfall event in Henan Province, China. *Sci. China Earth Sci.* **2022**, *65*, 1879–1902. [CrossRef]
66. Zhang, Y.; Yu, H.; Zhang, M.; Yang, Y.; Meng, Z. Uncertainties and error growth in forecasting the record-breaking rainfall in Zhengzhou, Henan on 19–20 July 2021. *Sci. China Earth Sci.* **2022**, *65*, 1903–1920. [CrossRef]
67. Zhang, F.; Bei, N.; Rotunno, R.; Snyder, C.; Epifanio, C. Mesoscale predictability of moist baroclinic waves: Convection permitting experiments and multistage error growth dynamics. *J. Atmos. Sci.* **2007**, *64*, 3579–3594. [CrossRef]

68. Selz, T.; Craig, G.C. Upscale error growth in a high-resolution simulation of a summertime weather event over Europe. *Mon. Weather Rev.* **2015**, *143*, 813–827. [CrossRef]
69. Hohenegger, C.; Schar, C. Atmospheric predictability at synoptic versus cloud-resolving scales. *Bull. Am. Meteorol. Soc.* **2007**, *88*, 1783–1793. [CrossRef]
70. Hohenegger, C.; Schar, C. Predictability and error growth dynamics in cloud-resolving models. *J. Atmos. Sci.* **2007**, *64*, 4467–4478. [CrossRef]
71. Done, J.M.; Craig, G.C.; Gray, S.L.; Clark, P.A. Case-to-case variability of predictability of deep convection in a mesoscale model. *Quart. J. Roy. Meteorol. Soc.* **2012**, *138*, 638–648. [CrossRef]
72. Flack, D.L.; Gray, S.L.; Plant, R.S.; Lean, H.W.; Craig, G.C. Convective-scale perturbation growth across the spectrum of convective regimes. *Mon. Weather Rev.* **2018**, *146*, 387–405. [CrossRef]
73. Keil, C.; Heinlein, F.; Craig, G.C. The convective adjustment time-scale as indicator of predictability of convective precipitation. *Quart. J. R. Meteorol. Soc.* **2014**, *140*, 480–490. [CrossRef]
74. Surcel, M.; Zawadzki, I.; Yau, M.K. The case-to-case variability of the predictability of precipitation by a storm-scale ensemble forecasting system. *Mon. Weather Rev.* **2016**, *144*, 193–212. [CrossRef]
75. Bachmann, K.; Keil, C.; Weissmann, M. Impact of radar data assimilation and orography on predictability of deep convection. *Quart. J. Roy. Meteorol. Soc.* **2019**, *145*, 117–130. [CrossRef]
76. Bachmann, K.; Keil, C.; Craig, G.C.; Weissmann, M.; Welzbacher, C.A. Predictability of deep convection in idealized and operational forecasts: Effects of radar data assimilation, orography, and synoptic weather regime. *Mon. Weather Rev.* **2020**, *148*, 63–81. [CrossRef]
77. Wu, P.-Y.; Takemi, T. The impact of topography on the initial error growth associated with moist convection. *SOLA* **2021**, *17*, 134–139. [CrossRef]
78. Wu, P.; Takemi, T. Impacts of mountain topography and background flow conditions on the predictability of thermally induced thunderstorms and the associated error growth. *J. Atmos. Sci.* **2023**, *80*, 1177–1199. [CrossRef]
79. Wang, X.; Yau, M.K.; Nagarajan, B.; Fillion, L. The impact of assimilating radar-estimated rain rates on simulation of precipitation in the 17–18 July 1996 Chicago floods. *Adv. Atmos. Sci.* **2010**, *27*, 195–210. [CrossRef]
80. Wilks, D.S. *Statistical Methods in the Atmospheric Sciences*, 3rd ed.; Elsevier: Amsterdam, The Netherlands, 2011; 676p.

Disclaimer/Publisher's Note: The statements, opinions and data contained in all publications are solely those of the individual author(s) and contributor(s) and not of MDPI and/or the editor(s). MDPI and/or the editor(s) disclaim responsibility for any injury to people or property resulting from any ideas, methods, instructions or products referred to in the content.